Draft 2

Precision Measurements of the Electromagnetic Properties of Pseudoscalar Mesons at 11 GeV via the Primakoff Effect

The PrimEx Collaboration

Contributing Editors:

A. Gasparian, L. Gan, J. Goity, M. Ito, D. Lawrence, A. Margarian, R. Miskimen, A. Bernstein, D. Dale

June 12, 2000

Contents

1 Introduction

The future availability of high quality, high duty factor 11 GeV electron beams at TJNAF will enable new, unprecedented opportunities to perform precise measurements of meson decay widths and electromagnetic transition form factors. Here, we detail how one can exploit the high energy electro- and photoproduction of pseudoscalar mesons in the Coulomb field of a nucleus, the so called Primakoff effect, to study the two photon decay widths, $\Gamma_{\gamma\gamma}$, and the transition form factors, $F_{\gamma\gamma^* P}$, where P represents the π^o, η, and η' pseudoscalar mesons. This comprehensive program will provide fundamental tests of both quantum chromodynamics and QCD inspired models.

In addition to the proposed 11 GeV upgrade to the CEBAF accelerator, this program will require the construction of some ancillary instrumentation including (1), a magnetic spectrometer for a virtual photon tagging facility, (2) a hybrid calorimeter for detection of multiphoton states and in some cases, scattered electrons, and (3) a recoil detector based on low pressure multiwire proportional chambers. The requirements for this instrumention and the physics which it will make possible are described below.

2 Motivation

The coupling of two photons to neutral mesons via their constituent quarks provides important information about their hadronic structure. Indeed the $\gamma\gamma P$ interaction, where P represents the $C = +1$ pseudoscalar mesons, is the most fundamental electromagnetic vertex, since the Coulomb form factor (γPP) vanishes due to charge conjugation symmetry. The C allowed $\gamma\gamma P$ coupling, however, is proportional to the fourth power of the quark charges, and can thereby provide a powerful tool to probe the charged parton content of the meson.

The three neutral pseudoscalar mesons π^0, η and η' represent in particular one of the most interesting systems in strong interactions. This system contains fundamental information about the effects of SU(3) and isospin breaking by the u, d, and s quark masses, leading to important mixing effects among the mesons. In addition, two types of chiral anomalies are involved, namely, the $U_A(1)$ anomaly that involves the flavor singlet axial current $j^\mu_A = \bar{q}\gamma^\mu\gamma_5 q$ and the color currents, and the anomalies involving either the singlet axial current or one of the two neutral axial currents ($j^\mu_{A3} = \bar{q}\gamma^\mu\gamma_5\lambda_3 q$ and $j^\mu_{A8} = \bar{q}\gamma^\mu\gamma_5\lambda_8 q$, where $q = (u, d, s)^T$) and two electromagnetic currents.

In the chiral limit, the classical QCD Lagrangian,

$$\mathcal{L}_{QCD} = \sum_{i=u,d,s} \bar{\psi}_i(i \not{\partial} - g \not{A} - m_i)\psi_i - \frac{1}{4}G^a_{\mu\nu}G^{\mu\nu}_a, \tag{1}$$

is invariant under both chiral $SU_L(3) \times SU_R(3)$-flavor transformations and axial $U_A(1)$ transformations. As a consequence of these symmetries, the Noether currents associated with infinitesimal axial transformations are conserved in the classical theory. In the full quantum field theory, however, these two symmetries are realized differently: chiral $SU_L(3) \times SU_R(3)$

is not only a symmetry of the classical QCD Lagrangian, but also a symmetry of the full quantum field theory. However, while the QCD Hamiltonian is invariant under chiral $SU_L(3) \times SU_R(3)$, this symmetry is spontaneously broken to $SU(3)$ in the ground state. As a result, there are eight massless Goldstone bosons corresponding to the eight spontaneously broken freedoms in the symmetry transformations: the octet pseudoscalar mesons (π^0, η, K, *etc.*). In reality, these Goldstone mesons are not massless because the quark masses are non zero (albeit small), thus breaking the symmetry explicitly.

Unlike chiral $SU_L(3) \times SU_R(3)$, the axial $U_A(1)$ is no longer a symmetry of the full quantum theory, even though it is a symmetry of the classical QCD Lagrangian. This is called the chiral anomaly, which has a pure quantum mechanical origin. The reason is because of the famous Adler-Bell-Jackiw anomaly:

$$\partial_\mu j_A^\mu = \frac{N_F \alpha_s}{8\pi} \varepsilon^{\mu\nu\lambda\sigma} G^a_{\mu\nu} G_{a\lambda\sigma} \tag{2}$$

where $N_F = 3$ is the number of flavors appearing in the axial current, and G is the gluon field. The $U_A(1)$ symmetry is explicitly broken by the quantum fluctuations of the quark fields coupling to a gauge field, representing one of the most profound symmetry issues in QCD. Thus, there is no Goldstone boson associated with the axial current. Consequently the η' meson, which has the same quantum numbers as the η, is not the Goldstone particle due to the anomaly.

There is a second type of $U_A(1)$ anomaly that involves the coupling of the quarks to the photon fields. This leads to a similar non-vanishing divergence to the $U_A(1)$ current:

$$\begin{aligned}
\partial_\mu j_{A3}^\mu &= \frac{N_c \alpha_{em}}{3\pi} \epsilon^{\mu\nu\rho\sigma} F_{\mu\nu} F_{\rho\sigma} \\
\partial_\mu j_{A8}^\mu &= \frac{1}{\sqrt{3}} \frac{\alpha_{em}}{3\pi} \epsilon^{\mu\nu\rho\sigma} F_{\mu\nu} F_{\rho\sigma}
\end{aligned} \tag{3}$$

where the $F's$ are the electromagnetic fields, and N_c is the number of colors in QCD. This anomaly plays a crucial role in the physics of the (π^0, η, η') complex, being directly responsible for the decays of the three mesons into photon pairs. In the chiral limit, the second type of anomaly leads to a rigorous prediction of the π^0, η and η' decay amplitudes into two photons:

$$\begin{aligned}
A(\pi^o \to \gamma\gamma) &= A_{\pi^0\gamma\gamma} \epsilon^{\mu\nu\rho\sigma} \epsilon_\mu \epsilon'_\nu k_\rho k'_\sigma \\
A(\eta \to \gamma\gamma) &= A_{\eta_8\gamma\gamma} \epsilon^{\mu\nu\rho\sigma} \epsilon_\mu \epsilon'_\nu k_\rho k'_\sigma \\
A(\eta' \to \gamma\gamma) &= A_{\eta_1\gamma\gamma} \epsilon^{\mu\nu\rho\sigma} \epsilon_\mu \epsilon'_\nu k_\rho k'\sigma,
\end{aligned} \tag{4}$$

where ϵ and k represent photon polarizations and momenta respectively, and $A_{\pi^o\gamma\gamma} = \frac{\alpha_{em}}{8\pi f_\pi}$, $A_{\eta_8\gamma\gamma} = \frac{\alpha_{em}}{8\sqrt{3}\pi \bar{f}_{\eta_8}}$, and $A_{\eta_o\gamma\gamma} = \frac{\alpha_{em}}{\sqrt{24}\pi \bar{f}_{\eta'_0}}$. The f's are the corresponding meson decay constants. While in the chiral limit SU(3) symmetry implies that $f_\pi = \bar{f}_{\eta_8}$, $\bar{f}_{\eta'_0}$ is not constrained by symmetries. However, in the limit of large number of colors in QCD (large N_c limit), one has $\bar{f}_{\eta 0} = f_\pi$.

In the chiral limit ($m_q \to 0$), the π^0 and η are Goldstone bosons belonging to an octet of SU(3) and their masses would vanish exactly, while the η' would be a singlet of SU(3) and acquire a mass due to the axial anomaly accompanied by the instanton configurations of the gluon fields. The relatively straightforward situation of the chiral limit becomes much more complex in the real world in which the quark masses are non-vanishing. In the real world the current quark masses are estimated to be $m_u \sim m_d/2 \sim 5$ MeV and $m_s \sim 150$ MeV. These masses make the π^0 and the η massive and shift the mass of the η' due to explicit breaking of chiral symmetry, while SU(3) and isospin breaking induce mixing among the three mesons. The mixing is expressed in terms of three mixing angles. Writing on the left the eigenstates of the chiral limit, we have:

$$\pi_8^0 = \pi^0 - \epsilon\eta - \epsilon'\eta'$$

$$\eta_8 = cos\theta(\eta + \epsilon\pi^0) + sin\theta(\eta' + \epsilon'\pi^0)$$

$$\eta_1 = -sin\theta(\eta + \epsilon\pi^0) + cos\theta(\eta' + \epsilon'\pi^0)$$

The mixing angle ϵ is predicted in ChPT to be approximately $-0.55°$. For the other two angles there are no rigorous predictions. If the large N_c limit holds without large corrections, then there is a prediction: $\epsilon' \sim -0.25°$ and $\theta \sim -22°$. It is so far unknown how large the deviations from the large N_c limit are, but expectations are that they are reasonably small. The angles ϵ and ϵ' play a role in the lifetime of the π^0, decreasing the lifetime by approximately 2%. For this proposal the relevant mixing angle is θ, and its value could be determined experimentally by the effect the mixing has on the decay rates of the η and η' into two photons:

$$\Gamma(\eta \to \gamma\gamma) = \frac{\alpha_{\rm em}^2}{64\pi^3}\frac{M_\eta^3}{3f_\pi^2}\left[\frac{f_\pi}{\bar{f}_{\eta 8}}\cos\theta - \sqrt{8}\frac{f_\pi}{\bar{f}_{\eta 0}}\sin\theta\right]^2 \quad (5)$$

$$\Gamma(\eta' \to \gamma\gamma) = \frac{\alpha_{\rm em}^2}{64\pi^3}\frac{M_{\eta'}^3}{3f_\pi^2}\left[\frac{f_\pi}{\bar{f}_{\eta 8}}\sin\theta + \sqrt{8}\frac{f_\pi}{\bar{f}_{\eta 0}}\cos\theta\right]^2 \quad (6)$$

where $\bar{f}_{\eta 8}$ is predicted in ChPT to be 1.3 f_π. For $\bar{f}_{\eta 0}$ there is no independent determination, and theory can only give a rough estimate based on large N_c, where $\bar{f}_{\eta 0} \sim f_\pi$. If one measures the decay widths of η, η' into two photons, both mixing angle and $\bar{f}_{\eta 0}$ can be determined. One can also define a mixing independent quantity, R, involving a combination of the π^0, η and η' widths and the decay constants $\bar{f}_{\eta 8}$ and $\bar{f}_{\eta 0}$ as follows:

$$R \equiv \left[\frac{\Gamma(\eta \to \gamma\gamma)}{M_\eta^3} + \frac{\Gamma(\eta' \to \gamma\gamma)}{M_{\eta'}^3}\right]\frac{M_\pi^3}{\Gamma(\pi^0 \to \gamma\gamma)} = \frac{1}{3}\left(\frac{f_\pi^2}{\bar{f}_{\eta 8}^2} + 8\,\frac{f_\pi^2}{\bar{f}_{\eta 0}^2}\right), \quad (7)$$

This quantity could be directly measureable with an 11 GeV beam at Jefferson Lab. Reference [3] quotes its current value with error bars to be $R_{exp} = 2.5 \pm 0.5(\text{stat}) \pm 0.5(\text{syst})$.

More precise measurements of $\Gamma(\eta \to \gamma\gamma)$ and $\Gamma(\eta' \to \gamma\gamma)$ are crucial to the understanding of the mixing of the two mesons and the decay constant $\bar{f}_{\eta 0}$. The measurements of the η width have been carried out using the Primakoff effect [?] and $\gamma - \gamma$ fusion in $e^+ - e^-$ colliders [?]. These determinations are in clear disagreement. The η' width, on the other hand, has only been measured in $e^+ - e^-$ colliders [?]. The current results for the widths are:

$$\Gamma(\eta \to \gamma\gamma)_{\text{Primakoff}} = 324 \pm 46 \text{ eV}$$

$$\Gamma(\eta \to \gamma\gamma)_{\text{Collider}} = 510 \pm 26 \text{ eV}$$

$$\Gamma(\eta' \to \gamma\gamma)_{\text{Collider}} = 427 \pm 0.19 \text{ eV}$$

Applying equation (5) and (6), one obtains respectively: $\theta = -16°$, $\bar{f}_{\eta_0} = 100$ MeV for the Primakoff η measurement, and $\theta = -22°$, $\bar{f}_{\eta'_0} = 95$ MeV for the collider case. This is clearly an unsatisfactory experimental situation. A new high quality Primakoff measurement of the η decay and a first Primakoff measurement of the η' can lead to a clarification and a precise determination of the mixing angle θ.

An improved $\Gamma(\eta \to \gamma\gamma)$ measurement will also shed considerable light on our understanding of the quark mass difference. The $\eta \to \pi\pi\pi$ partial width is determined through the $\Gamma(\eta \to \gamma\gamma)$ radiative width and the $\eta \to \pi\pi\pi$ branching ratio, and in the lowest order chiral Lagrangian, the amplitude of $\eta \to 3\pi$ is proportional to the quark mass difference $m_d - m_u$. The current uncertainty in the $\eta \to \pi\pi\pi$ partial width is dominated by the uncertainty in the η radiative width. As we will argue below, considerable improvement in our knowledge of the $\eta \to \gamma\gamma$ width can be obtained with the availability of 11 GeV beams at TJNAF.

Using Primakoff electroproduction it is also possible to gain access to the transition form factors $F_{\gamma\gamma^* P}$ for one off shell photon. So far, the transition form factors have been determined in collider experiments [?], where $Q^2 \geq 0.6$ GeV^2, except for the form factor for the η' measured by the L3 collaboration where Q^2 is as low as 0.05 GeV^2 but with big error on Q^2. Measurements of the π^0, η and η' transition form factors at very low Q^2 ($\sim$ 0.001–0.5GeV^2) will allow one to extract the slope of the transition form factor, and model independently measure the size of the meson's electromagnetic interaction radius. Currently, there is no first principles theoretical determination of the form factors. In ChPT there are two sources of contributions [?], one is the long distance contribution from meson loops, and the other is a counterterm or short distance contribution. ChPT pins down the first, and for the second a model is needed. The long distance contributions are small, as they only provide a small fraction of the fall off of the form factor. The simplest model is to neglect the long distance contributions and assume a monopole type form factor,

$$F(Q^2) = \frac{\Lambda^2}{Q^2 + \Lambda^2}.$$

using such a model, the available data fits very well with a scale $\Lambda \sim 0.75 - 0.85$ GeV. The vector meson dominance (VMD) model is therefore an excellent model to fit the current data ($Q^2 > 0.6GeV^2$).

A determination of the slope of the π^0 and η form factors would allow one to uniquely fix a low energy constant $\mathcal{O}(p^6)$ in the effective chiral Lagrangian [?]. If the η' form factor slope can also be measured, then one could also have a clear test of how good the U(3) flavor symmetry implied by the large N_c limit holds. In this limit the same low energy term of order six should determine all slopes.

QCD purports to be the ultimate theory explaining all strong interaction effects at all energies and these are central issues of the theory. While asymptotic freedom is the most outstanding feature of the strong interaction at high energies, low energy QCD is more challenging theoretically since traditional perturbation theory breaks down. Chiral theory provides a framework for understanding the very low energy limit of QCD. At the lowest possible energies, the Standard Model involves only photons, electrons, muons and pions, as these are the lightest particles in the spectrum. Therefore, pion physics has a higher level of rigor than others because the chiral symmetry predictions more precisely describe nature in such an energy region. The predicted anomalous $\pi^0 \to \gamma\gamma$ amplitude[?, ?] is found by expanding the QCD chiral Lagrangian to first order in the pion field, yielding

$$A_{\gamma\gamma} = \alpha N_c/(3\pi f_\pi) = 2.513 \cdot 10^{-2} GeV^{-1} \tag{8}$$

where N_c is the number of colors in QCD, and $f_\pi = 92.42 \pm 0.25 MeV$ [?] is the pion decay constant. The number given above is for the accepted value of $N_c = 3$. The crucial aspect of this expression is that it has no free parameters that need to be determined phenomenologically. As a result, the width of $\pi^0 \to \gamma\gamma$ decay measurement is widely recognized as an important test of QCD, both as a measurement of the number of colors and also as a reflection of the symmetries and anomalies of the theory.

As the energy increases, the next degree of freedom will involve heavier mesons, such as the $\eta(549)$ and $\eta'(960)$. Theoretical predictions at this energy level require higher order corrections in the chiral Lagrangian. Some dependence on 'harder' physics remains in the form of the constants (a_i^r). They are not calculable from the symmetry structure and must be determined phenomenologically from the experimental data, in a similar way that high energy QCD has some dependence on 'soft' physics in the form of structure functions, fragmentation functions, *etc.* The proposed measurement of the mixing angle of the η and η' caused by the $SU(3)$ symmetry breaking, and the parameters in the antisymmetric $\mathcal{O}(p^6)$ chiral Lagrangian, are among those fundamental inputs to the Standard Model.

Among the pseudoscalar mesons, the η' plays a special role. As discussed earlier, because of the chiral anomaly the η' is a non-Goldstone boson which distinguishes it from the octet pseudoscalar mesons (π^0,η, *etc.*). There are a number of important and interesting issues remaining regarding the η'[4]:

- *In terms of quark and gluon degrees of freedom, what physical mechanism is responsible for the high η' mass?* So far, this is still an open question. In the chiral limit the η' mass is given in terms of the so called topological susceptibility. This susceptibility is of non-perturbative origin, and therefore difficult to calculate from first principles. So far some attempts have been made using lattice QCD, but the results remain uncertain. As the η' is a flavor singlet, some quark models suggest that it may mix with gluonic components through "pure glue" states, or higher Fock components where the meson consists of a quark and antiquark and a gluon. The first case will lower the η' mass, while in the second case the instantaneous annihilation interaction can act repulsively increasing its mass. Theoretically it is not clear for the moment which of these two effects is more important, and how much the gluonic component would be expected to be in the η'. Since the gluon does not carry charge, it cannot couple to photons. Therefore such gluon mixing in the η' would affect its two-gamma decay width. Analyzing the η and η' two-gamma decay widths and their transition form factors[5] will provide clarification on this issue.

- *Is the η' the would-be Goldstone boson?* For the analysis as well as interpretation of many experiments involving the η', it is necessary to know certain transition matrix elements. When lacking enough detailed knowledge about the microscopic structure of the η', one of the most powerful tools is symmetry. Without the anomaly, the η' would be like a pion with different flavor quantum numbers, so that symmetry arguments would be applicable. Can the η' be treated as the would-be Goldstone boson? Comparing the decay constant of the η' ($\bar{f}_{\eta 0}$) determined from η and η' two-gamma decay measurements with the one determined by making use of its would-be Goldstone boson nature, will help us gain model independent insight into the structure of η'.

In summary, the appearance of the chiral anomaly and the prediction of the Goldstone bosons due to the spontaneous breaking of chiral symmetry are two basic characteristics of QCD at low energies. Understanding the properties of pseudoscalar mesons which involve both Goldstone bosons and the chiral anomaly are fundamentally important in confinement scale QCD. The three neutral pseudoscalar mesons π^0, η and η', with the first two being Goldstone bosons whose masses vanish in the chiral limit, while the η' is not due to the chiral anomaly, represent one of the most interesting systems in low energy QCD. This system contains fundamental information about the effects of SU(3) and isospin breaking by the u, d, and s quark masses, leading to important mixing effects among the mesons, as well as about two types of chiral anomalies. A study of the two-photon decays of the π^0, η and η' and their transition form factors at very small Q^2 will allow one to determine the η, η' mixing angle and one constant $\mathcal{O}(p^6)$ in the chiral Lagrangian, and provide a test of the low energy limit of QCD in a relatively clean setting. In addition, a high quality measurement of the η two-gamma decay width will enlarge our knowledge of the $m_d - m_u$ quark mass difference by improving the precision of the $\eta \to \gamma\gamma$ width. The study of the η' will lead to a better understanding of the η' mass puzzle. As the lifetimes of the η and η' listed in the Particle Data Book were determined by the two-photon decay widths of those particles, these proposed measurements will give a better understanding of the properties of the η and η' in general.

3 Radiative Widths of Pseudoscalar Mesons

In January 1999, TJNAF PAC15 approved an experiment (E99-014, primEx collaboration) with A^- rating to perform a measurement in Hall B of the π^o lifetime using photoproduction in the Coulomb field of a nucleus. The proposed measurement at the $\simeq$1.4% accuracy level fills this important experimental gap between theory and experiment, and is arguably one of the most fundamental experiments that can be performed with few GeV electrons. New possibilities to measure the analogous decay widths for the η and η', however, will open up with the availability of 11 GeV beams. These are described below.

3.1 Previous Measurments of the η and η' Radiative Widths

The present experimental knowledge of the η meson width is presented in figure 1[**?**], along with the projected measurement which could be made with 11 GeV at Jefferson Lab. Most of the measurements in the figure have been performed using two photon interactions in e^+e^- collisions. One exception is the Cornell measurement of the η width[**?**] via the Primakoff effect. This gives a width which is significantly lower (at the 3σ level) than those from e^+e^- collisions. Using the same apparatus, the Cornell group measured the $\Gamma(\pi^0 \to \gamma\gamma) = 7.93 \pm 0.39$ eV, in good agreement with the world average value of 7.3 ± 0.2 eV, which is dominated by the collision experiments. As such, the η width should be remeasured by the Primakoff process using state-of-the-art experimental techniques to resolve this discrepancy.

The present status of the η' meson width is presented in figure 2[**?**], with the last point being the projected measurement at Jefferson Lab. All previous measurements use the $e^+e^- \to e^+e^-\gamma^*\gamma^* \to e^+e^-\eta'$ process, and the formation of the η' is identified by measuring its decay particles. As the branching ratios of the η' decay are known at only the $\sim 5\%$ level, the precision of these measurements is limited by these uncertainties. As a result, an alternative approach is strongly desirable. In the next section, we describe a technique in which the η' is tagged by the recoiling nucleus, thus obviating the need to know the branching ratios.

The horizontal lines in figure 1 and figure 2 show the sensitivity of the η and η' two photon decay widths to the $\eta - \eta'$ mixing angle. Venugoapl and Holstein[**?**] have determined the $\eta - \eta'$ mixing angle by simultaneuosly fitting data from η,η' reactions involving the anomaly $(\eta, \eta' \to \gamma\gamma, \pi^+\pi^-\gamma)$.Their result, $\theta = -20.8^o \pm 3.2^o$, is shown in the figures. It can be seen that the mixing angle is strongly dependent on the widths of η and η'. An improved measurement will provide an important constraint on this parameter. In addition, the figures also indicate that the η and η' two photon decay widths have opposite correspondency to the mixing angle. This would allow one to cross check the experimental systems if one measures both the η and η' two-gamma decay widths.

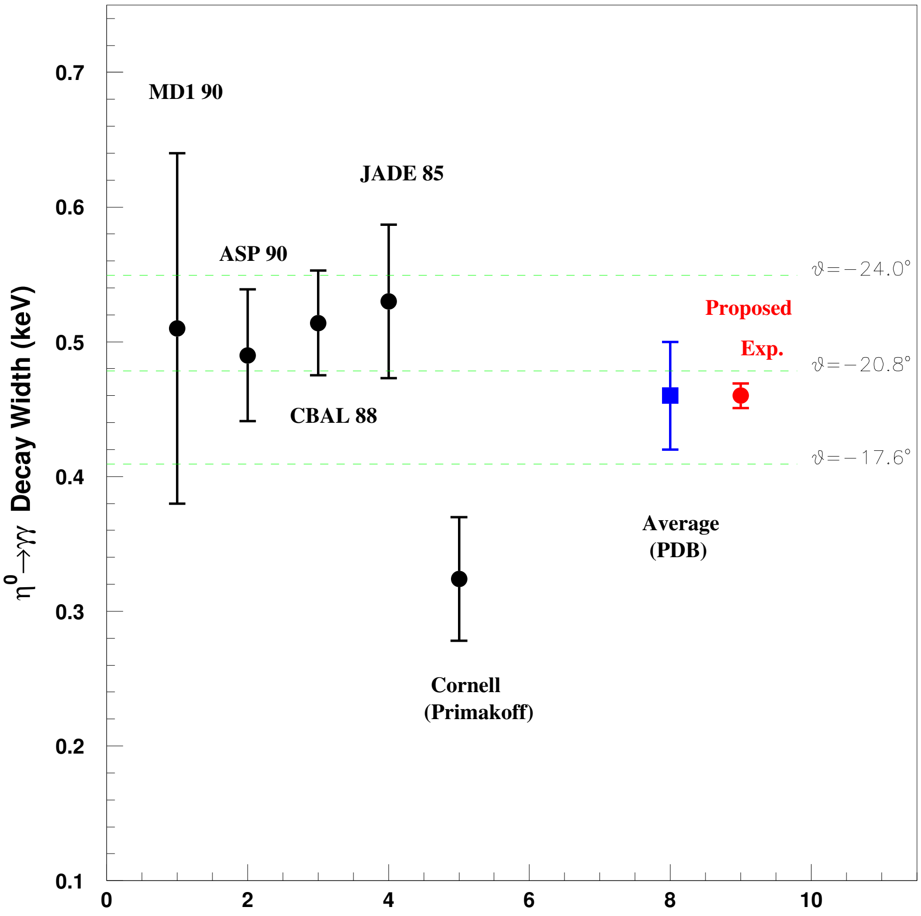

Figure 1: Two-photon decay width for the η meson. Points 1 through 4, are the results of e^+e^- collisions (for references, see[?]), point 5 is the result of a Primakoff experiment[?]. Point 6 is the Particle Data Book[?] average based on the first five points. Point 7 is the expected error for our future experiment, arbitrarily plotted to agree with the Particle Data Book average value. The plotted uncertainties combine the statistical and systematic errors in quadrature. The three lines are the widths for different η-η' mixing angles as indicated. See reference[?].

3.2 Measurement of the η and η' Radiative Widths via the Primakoff Effect

We propose to use a nearly real tagged photon beam obtained from 0° degree scattering of 11 GeV electrons to measure the widths of the $\eta, \eta' \to \gamma\gamma$ decays, via the Primakoff effect. The Primakoff effect is shown in figure 3. Mesons are produced by the interaction of a real or virtual photon with a virtual photon from the Coulomb field of the nucleus. The formation of mesons will be identified through missing mass reconstruction by measuring the recoil nucleus. The invariant mass and angle of the η will be reconstructed by detecting the η decay photons from the $\eta \to \gamma\gamma$ reaction.

The production of mesons in the Coulomb field of a nucleus by real photons is essentially the inverse of the decay $\eta, \eta' \to \gamma\gamma$, and the cross section for this process thus provides a measure of the η, η' two-photon decay widths.

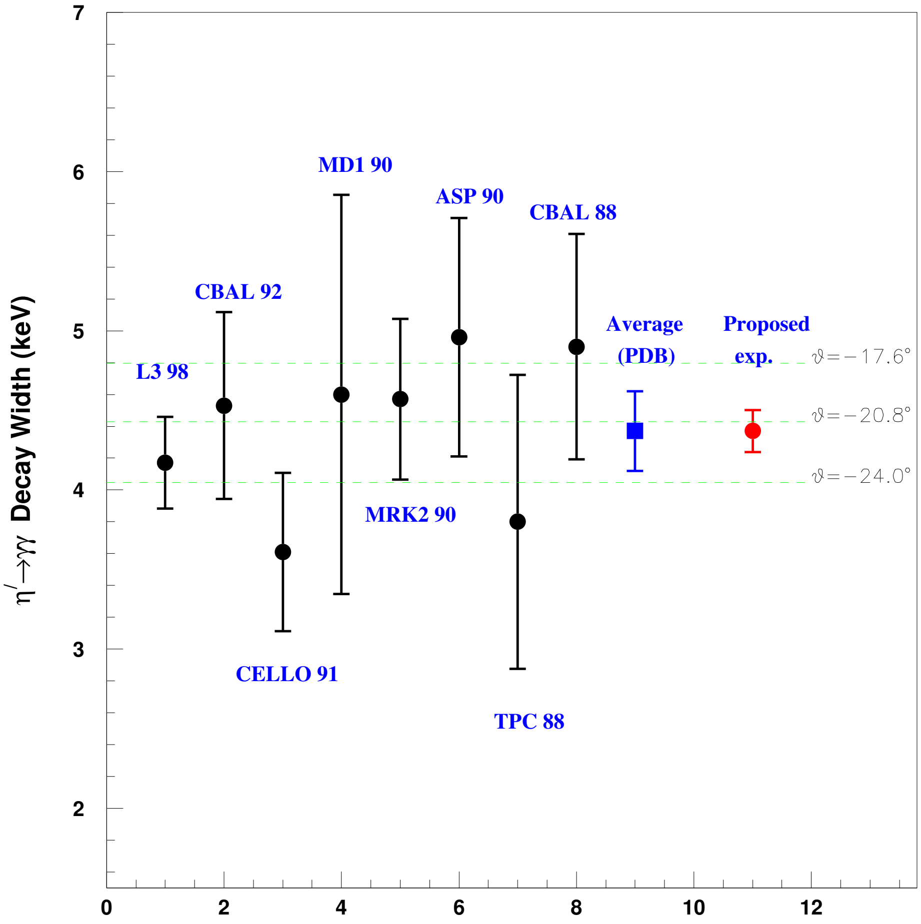

Figure 2: Two photon decay width for the η' meson. First 8 points are the results of e^+e^- collision experiments (for references see[?]). Point 9 is the Particle Data Book average based on the first 8 points. The last point is expected error of the proposed future experiment. The plotted uncertainties combine the statistical and systematic errors in quadrature. The three lines are the widths for different $\eta - \eta'$ mixing angles as indicated.

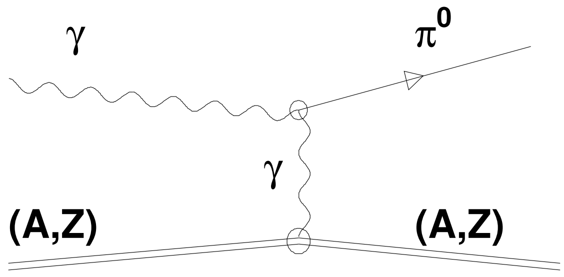

Figure 3: Schematic representation of the Coulomb photoproduction of neutral mesons (Primakoff effect).

For unpolarized photons, the Primakoff cross section is given by[**?**]:

$$\frac{d\sigma_P}{d\Omega} = \Gamma_{\gamma\gamma}\frac{8\alpha Z^2}{m^3}\frac{\beta^3 E^4}{Q^4}|F_{e.m.}(Q)|^2 sin^2\theta_m \tag{9}$$

where $\Gamma_{\gamma\gamma}$ is the decay width of the η or η', Z is the atomic number, m, β, θ_m are the mass, velocity and production angle of the mesons, E is the energy of the incoming photon, Q is the momentum transferred to the nucleus, and $F_{e.m.}(Q)$ is the nuclear electromagnetic form factor, corrected for final state interactions of the outgoing η or η'.

The Primakoff effect is not the only mechanism for meson photoproduction at high energies. There is coherent background from strong production of η,η' in the nuclear hadronic field, and an interference between the strong and Primakoff production amplitudes. The full cross section is given by:

$$\frac{d\sigma}{d\Omega_\pi} = \frac{d\sigma_P}{d\Omega} + \frac{d\sigma_C}{d\Omega} + \frac{d\sigma_I}{d\Omega} + 2\cdot\sqrt{\frac{d\sigma_P}{d\Omega}\cdot\frac{d\sigma_C}{d\Omega}}cos(\phi_1+\phi_2) \tag{10}$$

where the Primakoff cross section, $\frac{d\sigma_P}{d\Omega}$, is given by equation (3). The nuclear coherent cross section is given by:

$$\frac{d\sigma_C}{d\Omega} = C\cdot A^2|F_N(Q)|^2 sin^2\theta_\pi \tag{11}$$

and the incoherent cross section is:

$$\frac{d\sigma_I}{d\Omega} = \xi A(1-G(Q))\frac{d\sigma_H}{d\Omega} \tag{12}$$

where A is the nucleon number, $Csin^2\theta_m$ is the square of the isospin and spin independent part of the neutral meson photoproduction amplitude on a single nucleon, $|F_N(Q)|$ is the form factor for the nuclear matter distribution in the nucleus9 (corrected for final state interactions of the outgoing mesons), ξ is the absorption factor of the incoherently produced mesons, $1 - G(Q)$ is a factor which reduces the cross section at small momentum transfer due to the Pauli exclusion principle, and $\frac{d\sigma_H}{d\Omega}$ is the η,η' photoproduction cross section on a single nucleon. The relative phase between the Primakoff and nuclear coherent amplitudes without final state interactions is given by ϕ_1 and the phase shift of the outgoing meson due to final state interactions in the final state is given by ϕ_2.

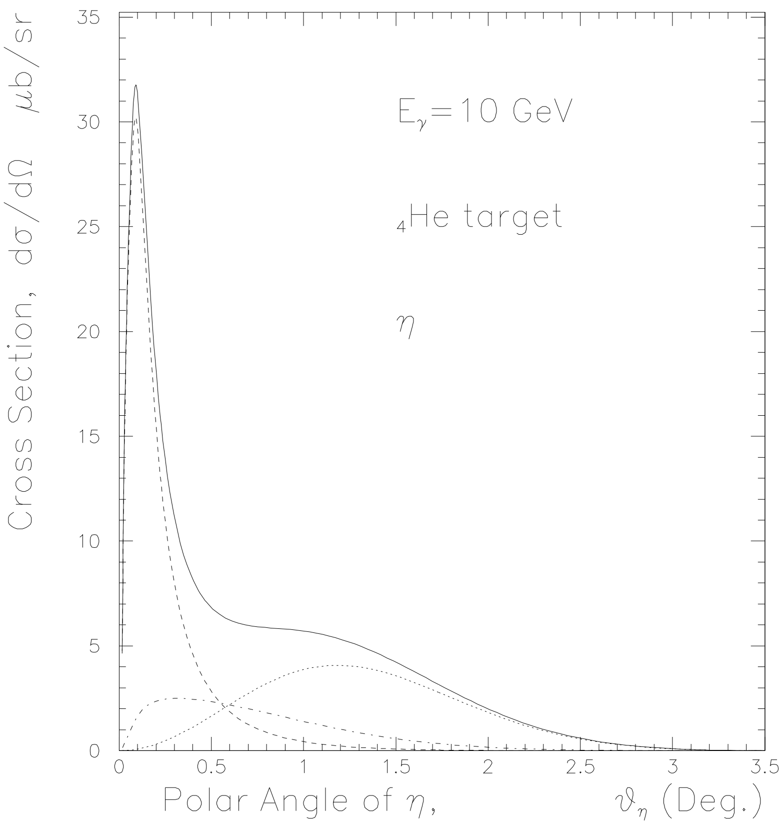

Figure 4: Differential cross sections (electromagnetic and nuclear) for the $\gamma^4He \rightarrow \eta^4He$ reaction at small angles at 10 GeV. The solid line is the total differential cross section from all the process, the dashed line is from Primakoff process, the dotted line is from the nuclear coherent process, and the dot-dash line is from the interference of the Primakoff and nuclear coherent processes.

Kinematical considerations enable one to separate Primakoff from other photo-meson production mechanisms. The Primakoff cross section is zero for mesons emitted along the incident photon direction (minimum four-momentum transfer t to the recoiling nucleus), has a sharp maximum at a very small angle (small t), and falls rapidly to zero at larger angles. It is proportional to Z^2, and its peak value is roughly proportional to E^4. The nuclear coherent cross section for spin zero nuclei is also zero in the forward direction, but has a broad maximum outside the angular region of the Primakoff effect, and falls at larger angles as shown in figure 4, where the amplitudes are normalized to the Cornell data[**?**]. The angular dependence (or t dependence) of the Primakoff signal and the background are different, allowing $\Gamma(\eta \to \gamma\gamma)$ and $\Gamma(\eta' \to \gamma\gamma)$ to be extracted from a fit to the angular distribution (or t distribution) of the photoproduced mesons. Measurements of the nuclear effects at larger angles are necessary to determine the unknown parameters in the production mechanism and thus make an empirical determination of the nuclear contribution in the Primakoff peak region. Consequently, to study the 2γ decay width of η and η' requires good angular resolution on the meson production angle, or good t resolution on the recoiling nucleus, to eliminate nuclear coherent production background.

Figure 5 shows t, the square of the four-momentum transferred to the nucleus, as a function of the meson production angles for the π^0, η and η'. The arrows indicate the locations of the Primakoff peaks. As one can see for the π^o, the Primakoff cross section is peaked at a very small t ($\sim 10^{-6}\ GeV^2$), so that the recoiling nucleus is likely to stay in the ground state. As the mass of the η and η' are higher than that of the π^0 however, the Primakoff cross sections are peaked at higher t (a few times $10^{-4}\ GeV^2$ for η and 10^{-3} GeV^2 for η'). As such, it becomes necessary to check the coherency of the meson production, especially for the case of the η'. A serious drawback of the previous Primakoff experiment[**?**] on $\Gamma(\eta \to \gamma\gamma)$ is that coherency was not established. As a result, recoil detection is required to ensure coherency and thereby distinguish backgrounds. In addition, as indicated in the previous section, in all the existing $\Gamma(\eta' \to \gamma\gamma)$ measurements, the signature of η' production is reconstructed by registering the decay particles from the η'. Consequently, poor knowledge of η' branching ratios ($\sim 5\%$) will limit the precision of the measurement. By tagging the η' through detection of the recoiling nucleus this uncertainty can be avoided.

As we are going to use the recoil detection technique, the target thickness must be thin enough to allow the recoiling nuclei to exit from the target. For such a thin target, tagging virtual photons at $0°$ represents a big advantage over real photon taagging because of the higher photon flux. Therefore, we propose using tagged zero degree virtual photons in the $\Gamma(\eta \to \gamma\gamma)$ and $\Gamma(\eta' \to \gamma\gamma)$ measurements.

The cross sections for the Primakoff effect to produce the η on ^4He is presented in figure 4. Compared to the Primakoff effect to produce the π^0, the η production has a significantly smaller cross section and peaks at larger production angles. This is a consequence of the much larger mass of the η which significantly increases the momentum transfer at a given production angle. As a result the Primakoff peak is harder to distinguish from the nuclear coherent peak. There are two ways to ameliorate this problem. One is to go to higher photon energies, which will help seperate the Primakoff signal from the background by pushing the Primakoff peak smaller angles and increase the Primakoff cross section ($\sigma_P \propto E^4$). As such, the proposed 11 GeV upgrade to the CEBAF accelerator is vital to these measurements.

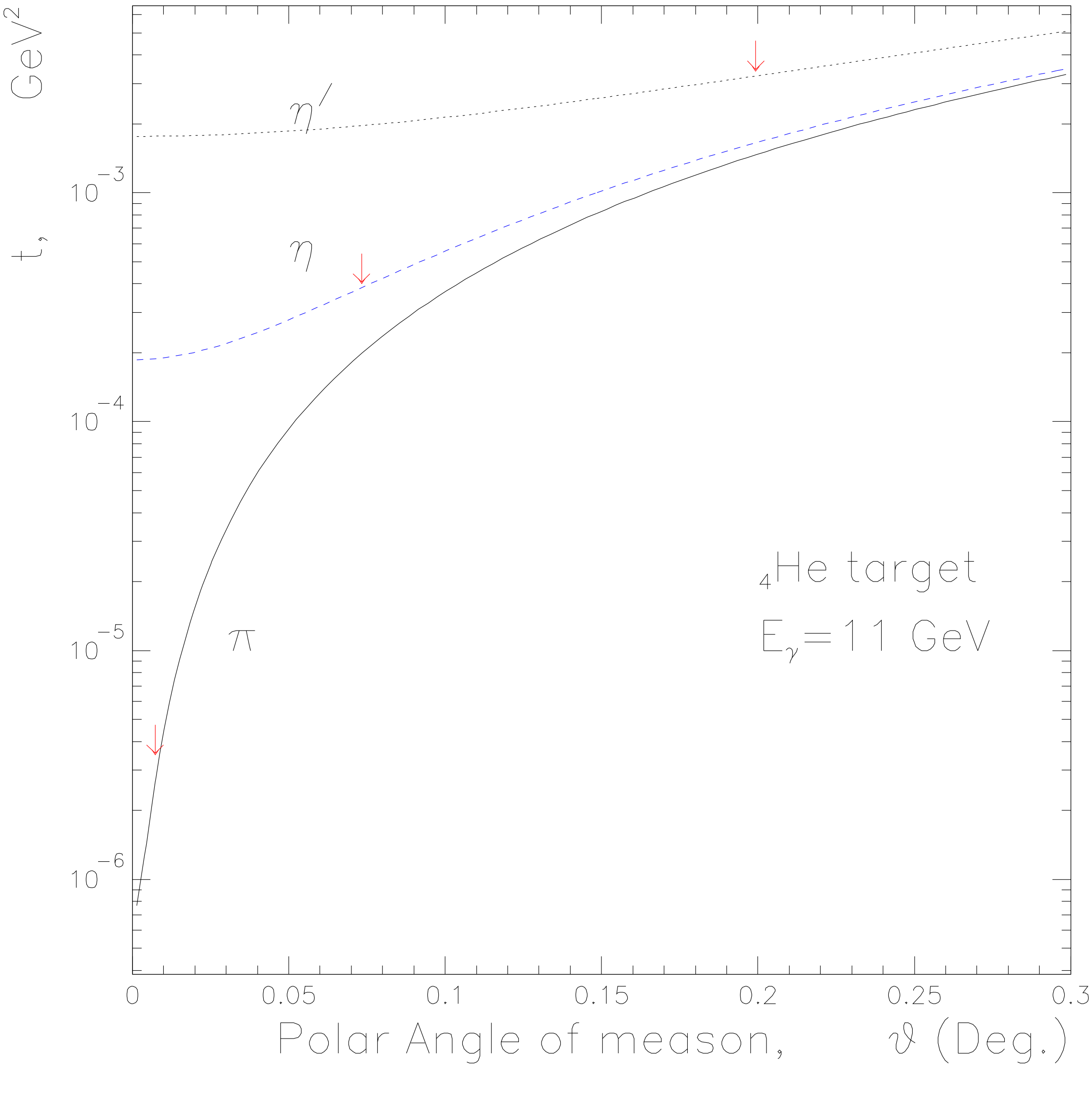

Figure 5: The four-momentum transfer to the nucleus t as a function of the meson production angles of π^0,η and η'. The arrows indicates the location of Primakoff peaks.

Another improvement is to use lighter targets such as ^{1}H, ^{4}He or ^{12}C, which are more stable compared to heavier nuclei, thereby enhancing coherency. We argue that by simultaneously going to higher photon energies and using lighter Primakoff production targets, one can make clean measurements of the widths.

3.3 Experimental Setup for η/η' Width Measurement

We propose to use the virtual photon tagging technique to produce the η/η' mesons, and to detect multiphoton final states in a hybrid calorimeter. In addition to the 11 GeV upgrade to the CEBAF accelerator, such measurements would require (1), a magnetic spectrometer for the virtual photon tagging system, (2), a low energy recoil detector based on low pressure multiwire proportional chambers to enable the separation of photoproduction via the Primakoff mechanism from other processes, and to identify the formation of mesons from missing mass reconstruction, (3) a $1.5m \times 1.5m$ multichannel hybrid calorimeter consisting of lead glass Cherenkov counters and a high resolution insertion in the central region composed of lead tungstate scintillating blocks, to detect decay particles from the meson decay, and (4), a small angle detector to enable the rejection of Møller and elastically scattered electrons. (see figure 6). The details of each instrument will be described below.

3.3.1 Zero Degree Virtual Photon Tagging System

In order to detect low energy recoiling nuclei from the target, very thin ($\sim 10^{-5}$ radiation length) targets are required. In this case, the virtual photon tagging technique holds a big advantage over real photon tagging. This is because, for the same electron tagging rate, the the ratio of the counting rate between the zero degree virtual photon tagger and the real photon tagger is given by[**?**]

$$\frac{R_{(0^0e,e'x)}}{R_{(tagged-\gamma,x)}} = \frac{t^V + t/2}{t} \tag{13}$$

where t^V is an effective virtual photon target thickness (~ 0.02), and t is the real photon target thickness. For a $\sim 10^{-5}$ radiation length of target,

$$\frac{R_{(0^0e,e'x)}}{R_{(tagged-\gamma,x)}} \sim \frac{0.02 + 10^{-5}}{10^{-5}} \sim 10^3 \tag{14}$$

which indicates that the virtual photon rate is about 10^3 times larger than real photon rate, while maintaining the signal to noise ratio at the same magnitude for the both virtual and real photon cases[**?**]. As pointed out by Hyde-Wright *et. al*[**?**], the signal to noise ratio will be optimized by operating near the bremsstrahlung endpoint, which will be the case in our experiment. The rates of the zero degree virtual photon tagging experiment will be limited by the electron singles rate in the electron spectrometer arm, which is dominated by the electrons from the bremsstrahlung process rather than by the reaction of interest.

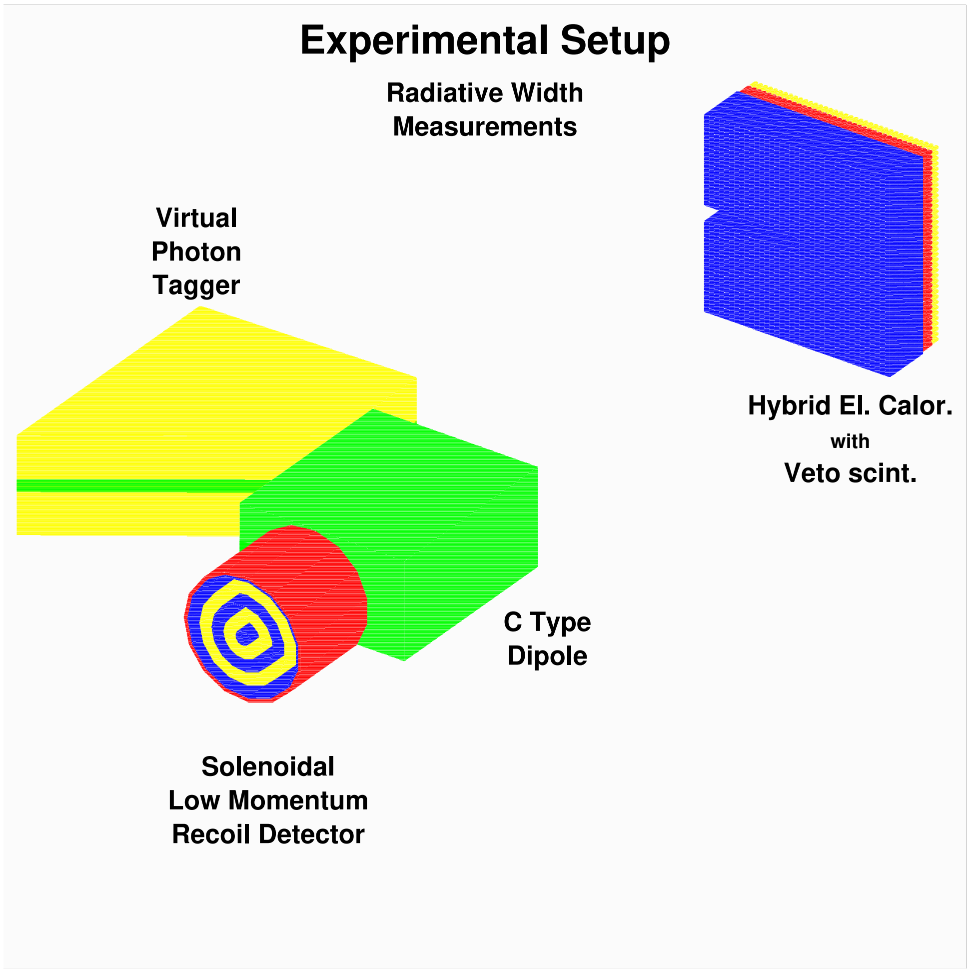
Experimental Setup
Radiative Width
Measurements
Virtual
Photon
Tagger
Hybrid El. Calor.
with
Veto scint.
C Type
Dipole
Solenoidal
Low Momentum
Recoil Detector

Figure 6:

The virtual photon flux factor Γ, which is the virtual number of virtual photons radiated per unit photon energy per unit electron solid angle per incident electron is[**?**]:

$$\begin{aligned}\Gamma(e_1,\omega,\theta) &= \frac{\alpha}{4\pi^2\omega}[\frac{e_1^2+e_2^2}{2e_1^2}(\frac{m^2\omega^2}{4e_1^2e_2^2}+sin^2(\frac{\theta}{2}))^{-1}-\frac{e_2m^2\omega^2}{e_14e_1^2e_2^2}(\frac{m^2\omega^2}{4e_1^2e_2^2}+sin^2(\frac{\theta}{2}))^{-2} \\ &\quad -\frac{(e_1+e_2)^2}{4e_1^2}(\frac{\omega^2}{4e_1e_2}+sin^2(\frac{\theta}{2}))^{-1}] \qquad (15)\end{aligned}$$

where e_1 and e_2 are the incident and scattered electron energies, θ is scattering angle, ω is photon energy, m is electron mass.

For an 11 GeV electron beam and 10.7 GeV tagged virtual photons, the flux factor distribution is shown in figure7. It can be seen that the virtual photons are mostly in the forward direction, and the intensity of photons falls rapidly with the scattering angle.

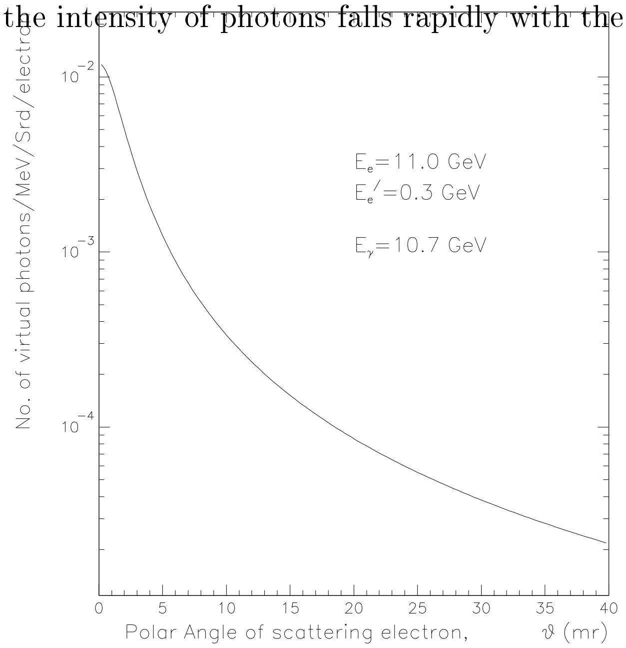

Figure 7: Calculated photon flux factor angular distribution.

The currently existing zero degree virtual photon tagger, the Enge spectrometer at TJNAF which was used in an HNSS hypernuclear spectroscopy experiment (Mar 1–May 14, 2000), can be used in our experiment with some minor modifications. The spectrometer is a split pole magnet designed by H. Enge[**?**]. The spectrometer parameters[**?**] are shown in Table 1. th eesolution without correction for the angle-position correlation is about 3×10^{-4}, so that only a focal plane detector package, a silicon strip detector and a segmented scintillator detector were used during the HNSS experiment for timing and particle identification as well as position determination. In the Primakoff experiment, we monitor the virtual photon flux by the electron scattering angle. Therefore, another off focal plane detector is needed in order to measure the electron scattering angle. During the HNSS experiment, the Enge spectrometer proved to be capable of running at electron singles rates of up to 1.5×10^8/sec, which is much higher than our requirement ($\sim 7 \times 10^6$/sec).

Momentum	240– 360 MeV/c
Design central momentum	276 MeV/c
Total Length	$\sim$ 5 m
Acceptance Solid angle acceptance Horizontal acceptance Vertical acceptance	 1.6 msr 25 mr 20 mr
Momentum bite	$\pm$20%
focal plane dimension Length Tilt Horizontal	 104 cm 42^o 80 cm
Momentum resolution	3×10^{-4}

Table 1: The parameters of the Enge spectrometer.

Figure 8 shows the photon flux distribution after passing through the Enge spectrometer acceptance, which was simulated by the RAYTRACE [?] program. It indicates that we may control the photon flux to better than 1% if the angular resolution is better than a few mr.

As the Enge spectrometer angular acceptance is relatively small, we are also keeping open the option to use another electron spectrometer which has a larger acceptance, so that we will be not sensitive to the spectrometer offsets.

3.3.2 Low-Energy Recoil Detection

a.)**Importance of Low-Energy Recoil Detection**

Detection of recoiling nuclei can offer important kinematical constraints on the reaction. Low-energy recoil measurements in Primakoff experiments performed in conjunction with measurements of the forward system allow one to:

- Separate the coherent process from incoherent background;
- Determine the four-momentum transfer to the nucleus (t) with high precision;
- Exclusively identify the formation of the mesons without detecting their decay particles.

A crucial parameter in the Primakoff process is the square of the invariant four-momentum, t, defined as

$$t = (p_o - p_i)^2 = (p_r - p_t)^2 \qquad (16)$$

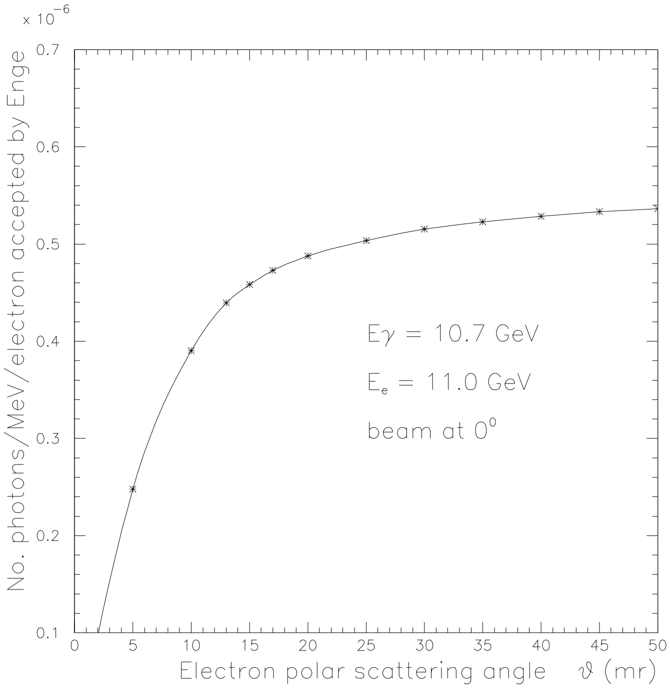

Figure 8: The photon flux distribution registered by Enge acceptance.

where p_i is the momentum of incident photon, p_o is the momentum of the outgoing meson (η or η'), p_t is the momentum of the target particle, and p_r is the momentum of the recoil nucleus. Assuming that the target is at rest ($p_t = 0$), in a coherent process ($m_r = m_t = M$), one obtains from the above definition:

$$t = (p_r - p_t)^2 = (E_r - M)^2 = -2MT, \tag{17}$$

where T is the recoiling nucleus' kinetic energy. Therefore the measurement error will be determined by:

$$\delta t = 2M \cdot \delta T \tag{18}$$

which shows that error in t is determined only by the uncertainty of T. Comparing this with the measurement of t from the forward angle spectrometer in the elastic process, at small scattering angles θ_o, t can be approximated by

$$-t \sim p_i^2 \cdot \theta_o^2, \tag{19}$$

For a known incident momentum p_i, the error in t is:

$$\delta t \sim 2p_i^2 \cdot \theta_o \cdot \delta\theta_o, \tag{20}$$

As one can see, t is determined by the error in the forward scattering angle, and is also proportional to p_i^2. When the incident momentum p_i increases, the error, δt, grows as well. As a result, determining the t through the recoil measurement has an advantage over measuring the forward scattering angle. As mentioned earlier, the recoil detection technique is also the only way to reach a measurement error of less than 5% in the case of the η' because of the poor knowledge of the η' decay branching ratio ($\sim 5\%$).

As the kinetic energy of the recoiling nucleus is low, a thin target is very important to allow recoiling nuclei to exit the target. Therefore one needs an intense beam to have a good production rate. As a result, the recoil detectors must have the ability to work in a high radiation environment. The properties of Low-Pressure Multiwire Proportional Chambers (LPMWPCs) and Low-Pressure Multi-Step Chambers (LPMSCs) [2,3] are appropriate to these goals. The main features of such chambers are summarized below:

- High rate capability ($\sim 10^5 Hz/mm^2$);
- Extreme insensitivity to gamma and neutron backgrounds;
- Capability to operate from an external gate, allowing the minimization of space charge effects;
- Negligible radiation damage;
- Good timing resolution ($\sim$ 200 ps, FWHM for fission fragments);
- Good position resolution ($\sim 200\mu m$, FWHM)
- High efficiency ($\sim$ 100%) for detecting low energy recoils;
- Negligible influence on the energy of recoils (the recoiling nucleus travels through the detectors with practically constant velocity).

b.) **Scientific Evaluation of the Low Pressure Chamber Technique**

During the past four years, a member of our collaboration (A. Margaryan) has been leading a group to develop LPMWPCs for a time-zero fission fragment (FF) detector for the direct measurement of the heavy hypernuclei lifetime at Jefferson Lab. The detector's characteristics and the method of time-zero reconstruction were investigated using fission fragments from a Cf-252 spontaneous fission source. It was shown that heptane, hexane, and isobutane gases at a pressure of 1-3 Torr are all suitable for such a fission fragment detector. As desired by experiment E95-002 (E99-003) [4], a timing and position resolution of about 200ps (FWHM) and $800\mu m$ (FWHM) for a chamber size of 21×21 cm^2 was achieved. In order to test the influence of the high radiation on the operation of the fission fragment detector, it was put in Hall C during E96-003 and E91-007 experiments near the beam at 7°, 20 meters downstream from a 4% radiator and a 12 cm liquid deuterium target. There were no noticeable changes in timing resolution of the detectors up to 10μA electron beam current, which produces 10^9 electrons/second in the solid angle of the chamber according to a Monte Carlo simulation [5]. At higher intensities (40-70 μA), the signals decreased 2-3 times due to space charge effects, but the time resolution of fission fragments from a Cf-252 source become worse by only 30% as shown in Fig. 9 and 10.

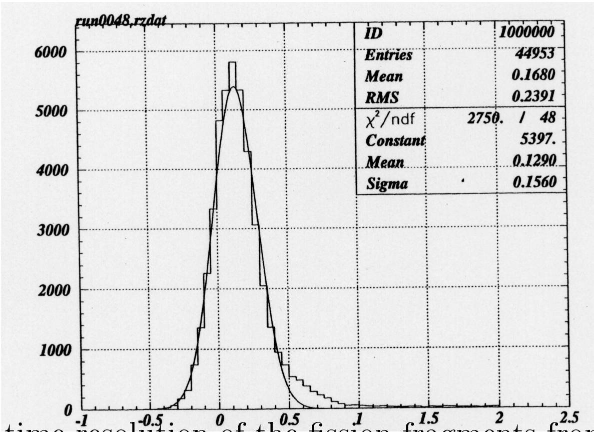

Figure 9: The time resolution of the fission fragments from a CF-252 source without beam.

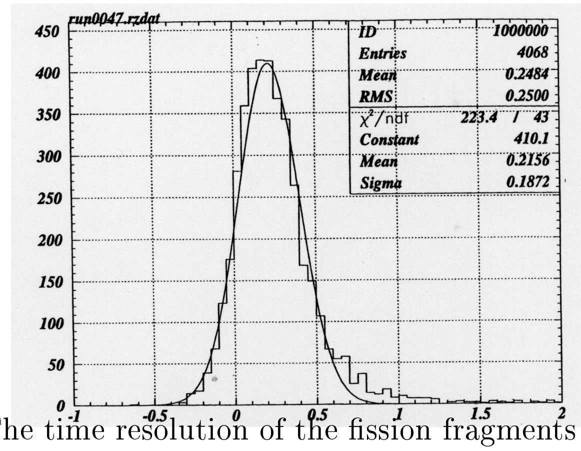

Figure 10: The time resolution of the fission fragments from a CF-252 source with beam.

In February 2000, during the commisioning of the HNSS hypernuclei experiment in Hall C, the chamber was put in front of the electron beam dump. There was no pile up when an approximately 1 μA, 1.8 GeV electron beam was passed directly through the chamber.

Similar techniques have been used for the measurement of the lifetime of heavy hypernuclei with the recoil shadow method and internal targets in the storage ring COSY-Julich [6]. Low pressure MWPCs have been operated at a distance of $\sim$ 30 cm from the target ($\sim$ 60 $\mu g/cm^2$) with $\sim 10^{10}$ protons at COSY and a cycle time of 10s. This internal target geometry corresponds to an external target experiment with an extracted beam of $\sim 1.6\mu A$ of 1.9 GeV protons.

The low-pressure technique has also been utilized to measure absolute electrofission and photofission cross sections [7,8]. In this case, the detectors were operated at a distance of ~ 20 cm from the targets ($\sim 500\mu g/cm^2$) at peak electron currents of ~ 10 mA (average currents were $\sim 0.5\mu A$)[8] or when a bremsstrahlung photon beam with intensity $10^9 - 10^{10}$ photon/sec passed directly through the detector with 30 mg/cm^2 Al plus 1.0 mg/cm^2 U target inside [8].

A large area detection system which consists of twelve LPMWPCs was used in the search for exotic super-massive nuclei [9]. Stable detector operation was reached even at the highest beam intensities, with electron currents in the detectors of at most 5 μA.

By means of this low-pressure technique it is possible to detect:

- Protons with energy 0.1– 5 MeV;
- Deuterons with energy 0.2–10 MeV;
- Alpha particles with energy 0.4 – 100 MeV;

as well as more heavy particles.

Coherent π^o electroproduction on ^4He was studied using the internal target facility of the AmPS electron storage ring at NIKHEF [10-11]. The experiment was performed at a luminosity of about $10^{33} cm^{-2}/s$ with a stored beam of about 200 mA (615 MeV and 676 MeV) electrons and a ^4He and ^2H gas target of 10^{15} atoms/cm^2. The neutral pions were detected by the coincidence of the scattered electrons with the recoiling ^4He nuclei measured by a dedicated recoil detector based on the low pressure technique [11]. This detector was designed to detect light ($A \leq 4$), low-energy (0.5–24 MeV for proton and 1–95 MeV for ^4He) nuclei.

As such, we conclude that the recoil detectors based on low-pressure MWPCs can be operated at a luminosity of up to 10^{33} cm^{-2}/s.

c.) **Recoil detector based on LPMWPCs**

The gas-filled magnetic spectrometer separator has been widely exploited in experimental nuclear physics [12-14]. This technique is suitable for the detection and identification of low-energy recoils. We suggest to use low-pressure heptane and hexane as a gas environment in the magnetic spectrometer-separator and as a working gas for the LPMWPCs or LPMSCs simultaneously. By means of the low-pressure technique, the time-of-flight and position parameters of the low energy recoils can be determined to within a few hundred picoseconds and a few hundred micrometer precision, and consequently one can determine their velocities and magnetic rigidities within a precision of a few percent. In addition, the dE/dx of low energy recoils can be measured. The resolving power of the gas-filled separator can be written as:

$$(A/\delta A)_{fwhm} = 100/(\delta(BR)/BR)_{fwhm}, \tag{21}$$

where A is the ion mass, BR is the magnetic rigidity in units of Tesla-meter, and $\delta(BR)/BR)_{fwhm}$ is in %. For a 2% total BR resolution,

$$(A/\delta A)_{fwhm} = 50; (Z/\delta Z)_{fwhm} = 30. \tag{22}$$

Z is the atomic number of the ion. Such a device will have wide application in intense electron beam experiments, providing the detection and identification of low-energy recoil nuclei in a wide range of mass and charges.

In the Primakoff process with a beam energy $\sim$ 11 GeV, the recoil kinetic energy is very low ($T_{min} \sim$ 0.5 MeV). The deposited energy of the recoil particles in the detector is comparable to the energy of recoils:

$$(dE/dx) \times \delta x \sim T \tag{23}$$

Thus the recoils can be identified by the measurement of the velocities V_1 and V_2, before and after the energy deposition:

$$A \times V_2^2/2 = A \times V_1^2/2 - (dE/dx) \times \delta x \tag{24}$$

and

$$A = \frac{2 \times (dE/dx) \times \delta x}{V_1^2 - V_2^2} \tag{25}$$

Figure 11 shows the range of the recoil ^4He and ^{12}C in a 1 Torr pressure Heptane gas for different kinetic energy. At $\sim$ 0.2 MeV kinetic energies, the range of ^4He is $\sim$ 35 cm and ^{12}C is $\sim$ 15 cm, which indicates that the recoil nuclei in such an energy range can travel enough distance to reach the detector.

We have a preliminary conceptual design of the recoil solenoid detector. It may consist of the following three elements: (1), a solenoid magnet; (2) the 3–5 internal layers of Low Pressure Multiwire Proportional Chambers (LPMWPCs) to detect the very low energy of the recoiling nuclei; (3), a solid state detector in the outer layers (silicon strip detector or segmented scintillator detector) for the higher energy recoil particles. The detector will cover the energy range $\sim$ 0.1–50 MeV for ^4He. Further research on this recoil detector is planned.

3.3.3 The Hybrid Calorimeter (HYCAL)

The electromagnetic decay particles from η and η', and scattered electrons in the transition form factor measurement will be detected in a highly segmented array of the Hybrid Shower Calorimeter (HYCAL) located downstream of the target. Currently our collaboration (PrimEx) is constructing a Hybrid Shower Calorimeter for an approved π^0 life time experiment in Hall B, as shown in figure **??**. We propose to use a somewhat larger version of this detector for the η and η' experiments. It will be about 150.0 x 150.0 cm^2 in the dimension transverse to the beam. The calorimeter is designed to measure both the position and the energy of electromagnetic showers using a two dimensional matrix of radiators (lead

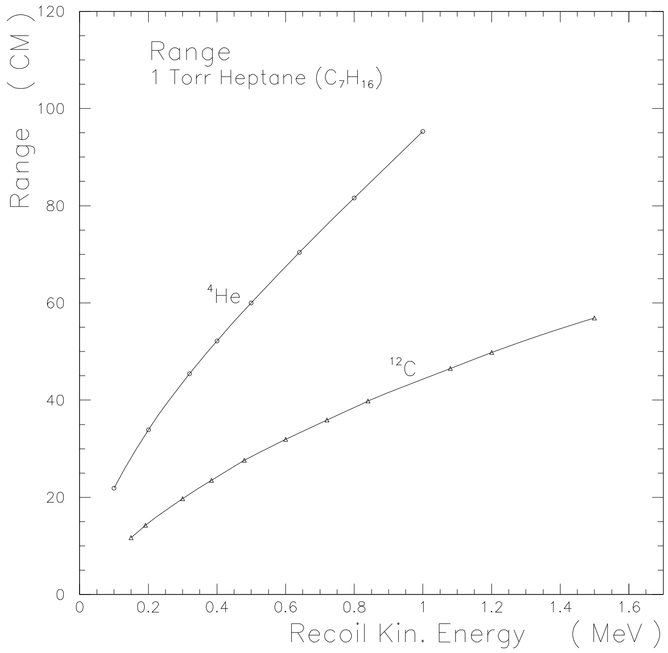

Figure 11: Range of ^4He and ^{12}C in heptane for different kinetic energy.

glass and crystals). That will be accomplished by choosing the cross section of the individual counters small enough so that the energy leakage into adjacent counters can be used to determine the position of the shower axis. The calorimeter will consist of two types of detectors. The outer part of the calorimeter will be made from lead glass Cherenkov detectors with the size of the radiators 4x4x40 cm^3.The excellent optical transparency and optimized transverse size of the lead glass radiator provide good energy and position resolutions:

$$\frac{\sigma_E}{E}(\%) = \frac{4.0}{\sqrt{E}} + 2.5, \sigma_x = \frac{5mm}{\sqrt{E}}, \tag{26}$$

where E is in GeV. As the Primakoff cross section peaks at extremely small angles: $\theta_\eta = 0.1^o$ at $E_\gamma = 10GeV$, in order to identify and extract the Primakoff amplitude (at very small recoil energy range, the formation of η will be determined by $\eta \to \gamma\gamma$ detection), the experimental setup must have sufficient resolution for the η production angle. This resolution depends strongly on the decay photon energy and position accuracy of the calorimeter. Therefore, the central region of the HYCAL will be constructed from lead tungstate ($PbWO_4$) crystals of size $2{\times}2{\times}20cm^3$. According to a recent report from the Mainz group, the energy resolution of similar crystals operated at a stabilized temperature (8°C) is:

$$\frac{\sigma_E}{E}(\%) = \frac{1.54}{\sqrt{E}} + 0.3, \tag{27}$$

where E is given in GeV[**?**]. These high resolution detectors will cover a $\sim 50 \times 50\ cm^2$ area around the beam where at least one photon from the $\eta \to \gamma\gamma$ decay will hit the central part of the calorimeter. In addition, this crystal insertion will significantly improve the radiation hardness of the detector near the beam line where radiation doses can be high. The central $12 \times 12cm^2$ hole will be left open to enable the photon beam to pass through. The modules contiguous with this region on the beam axis as well as the two outermost layers of modules in the lead glass wall will be excluded from the fiducial volume of the detector to control coordinate resolution and detection efficiency near the boundaries of the detector. To monitor and correct possible gain changes due to temperature and aging, a light monitoring system will be used. Details of the detector design can be found in the Conceptual Design Report of the π^0 life time measurement experiment.

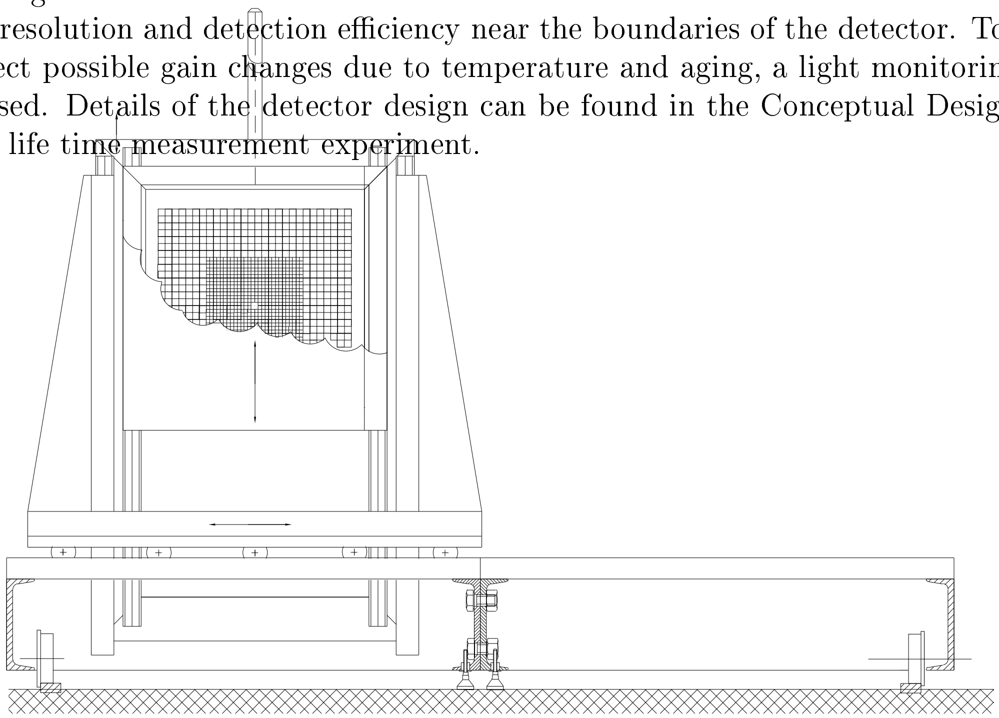

Figure 12: Schematic view of the HYCAL electromagnetic calorimeter with the transporter.

3.3.4 Background Veto Detector

The main source of background in the recoil detector arises from the recoiling nuclei from elastic electron scattering in the target, and the main background in the hybrid calorimeter is the Møller electrons. Offline, we will be able to distinguish the recoil events from η and η' production, which are of interest, from the elastic background. This is because their kinematics are very different. As shown in figure 13 and 14, the elastic recoil angle is located near 90^0, while the meson's production angle is smaller. The Primakoff cross section is peaked at a recoil angle of around 40°. On the other hand, the Møller events are also kinematically different from the η and η' decay events in the calorimeter. The Møller events consist of two charged electrons with total energy equaling that of the beam energy, while the η and η' decay events are usually accompanied by at least one γ. This allows one to separate them offline. Online, we will use a background veto detector to cut down both elastic and Møller background at the trigger level. (see figure 15). In addition, the prescaled elastic events can also be used to calibrate the recoil detector and monitor the luminosity.

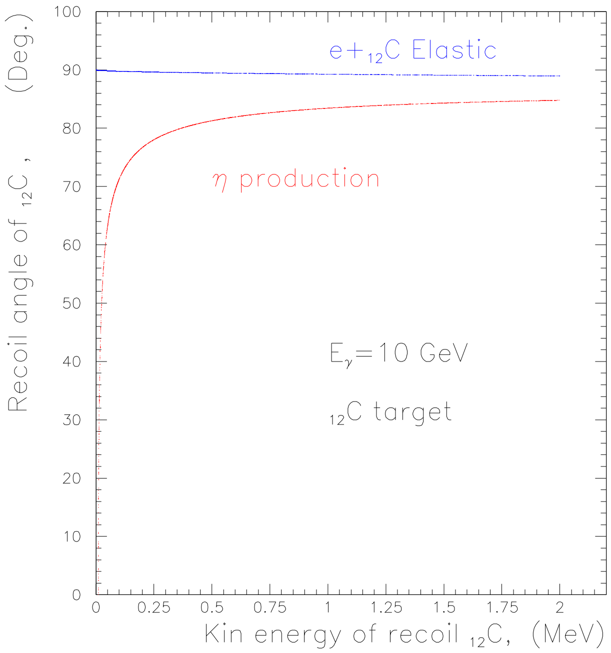

Figure 13: Kinematics of recoil ^{12}C from the η production reaction and elastic scattering.

We estimate the rates by assuming a 1μA electron beam ($N_e \sim 6.26 \times 10^{12}$ electron/sec), impinging upon a 40 cm heptane (C_7H_{16}) gas target at 1 torr, which corresponds to $N_{^{12}C} \sim 10^{19}\ atoms/cm^2$. The elastic scatttering cross section is:

$$\sigma_{el} = \int_{0.02MeV}^{\infty} \frac{d\sigma}{dT}(e,^{12}C)dT \sim 6.0mbarn \tag{28}$$

Therefore, the total elastic background rate from ^{12}C is:

$$\begin{aligned} N_{elastic} &= N_e \cdot N_{^{12}C} \cdot \sigma_{el} && (29) \\ &= 6.25 \times 10^{12} \times 10^{19} \times 6 \times 10^{-27} && (30) \end{aligned}$$

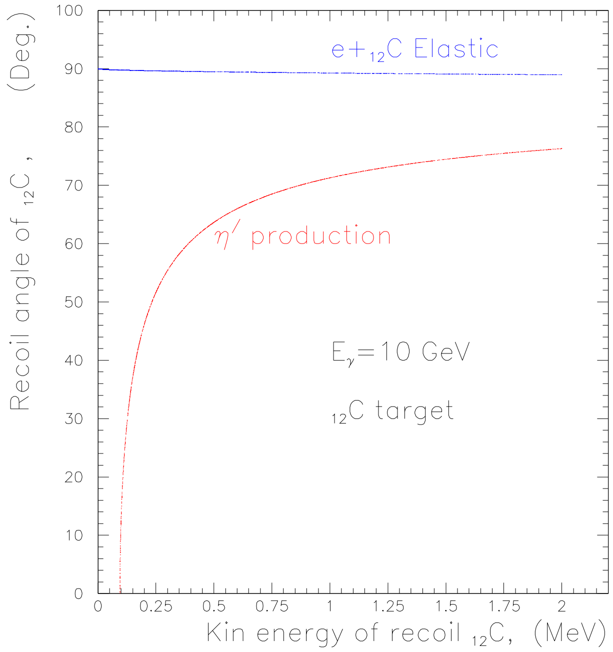

Figure 14: Kinematics of recoil ^{12}C from η' production reaction and elastics scattering.

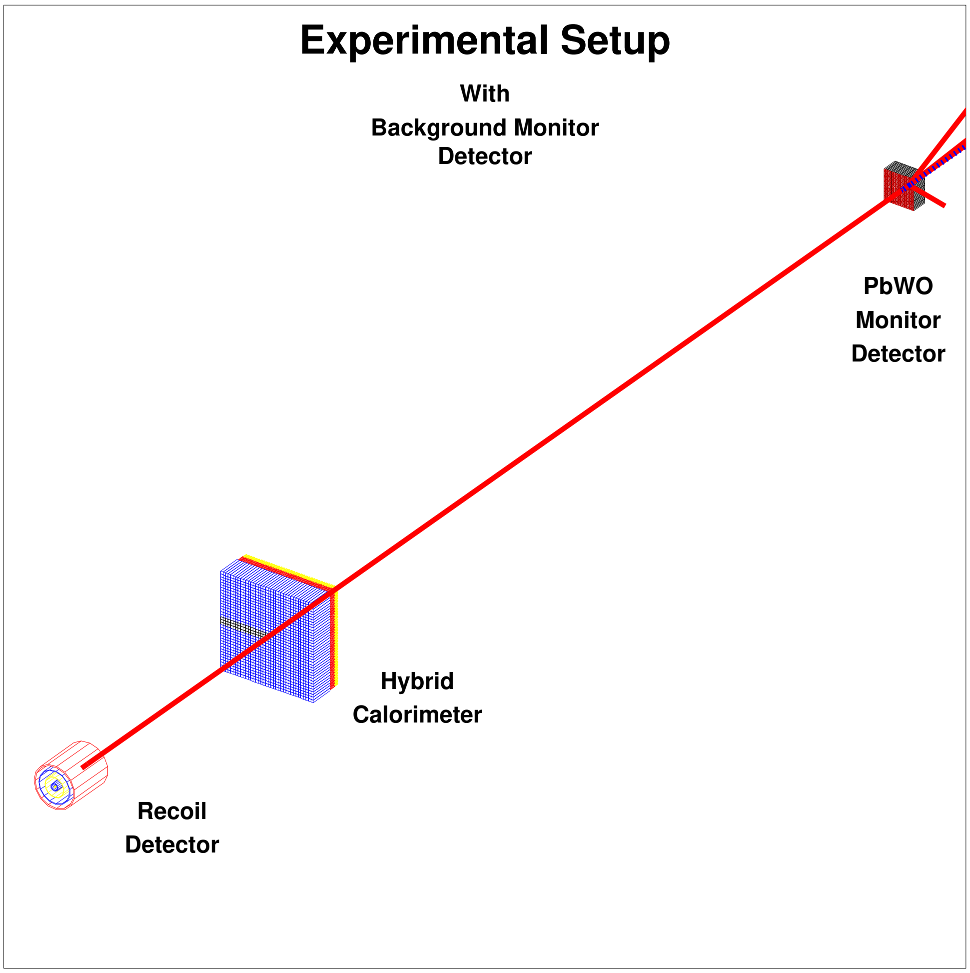

Figure 15: Background veto detector setup.

$$\sim \quad 4. \times 10^5 Hz \tag{31}$$

On the other hand, for a $150cm \times 150cm$ hybrid calorimeter with $12cm \times 12cm$ central hole to allow the beam to pass through, located $\sim$ 5 meters downstream from the target, the Møller electron background rate on the calorimeter is $\sim$ 67 kHz. In order to veto both elastic and Møller background at the trigger level, we will build a background veto detector, located $\sim$ 20 meters downstream of the target. It will be about 50×50 cm^2 in the dimension transverse to the beam, with a $4 \times 4cm^2$ hole in the middle. The detector will be constructed from lead tungstate ($PbWO_4$) cystals of size $2 \times 2 \times 20cm^3$.

Figure 3.3.4 shows the Monte Carlo result from a total of 22,000 elastic $(e,^{12}C)$ events. In the figure, (a) shows the elastic electron hit distribution on the hybrid calorimeter without any cut with 44 out of 22000 total events, which means the elastic background will have a very small effect on the calorimeter because of the small electron scattering angle; Figure (c) shows the elastic electrons hitting the background veto monitor detector, with 19956 out of 22000 events; Figure (b) shows the kinetic energy spectrum of recoiling ^{12}C nuclei from elastic scattering before the veto monitor cut, which indicates that the recoil background from the elastic scattering is mostly at small recoil energy. Figure (d) shows the kinetic energy spectrum of the recoiling ^{12}C nuclei from elastic scattering after the veto monitor cut, with only 44 out of 22000 events left. Therefore, the elastic background in the recoil detector is reduced 2×10^{-3} times by the veto monitor. For a 1μA electron beam, we will have a $4 \times 10^5 \times 2 \times 10^{-3} \sim 800Hz/\mu A$ elastic background left in the recoil detector and the calorimeter after the cut, and the elastic rate on the veto monitor is about 400 KHz per μA electron beam current.

Figure 17 shows the Monte Carlo result simulated from a total of 20,000 Møller events. In the figure, (a) and (c) show the position distribution and energy spectrum of Møller electrons hitting the hybrid calorimeter before the veto monitor cut, and the total hits on the detector is 13512; (b) and (d) show the position distribution and energy spectrum of Møller electrons on the hybrid calorimeter after the veto monitor detector cut, about 395 events left compared with before the cut, and (d) also indicates that only very small energy Møller events can survive from the veto detector cut, which can be cut eventually by setting detector energy threshold to about 1 GeV.

According to the cross section, the Møller event rate is about 10^5 Hz per 1μA electron beam. Thus, without a veto monitor cut, the Møller event rate on the calorimeter will be:

$$N_m \sim 1. \times 10^5 \times \frac{13500}{20 \times 10^3} \tag{32}$$

$$\sim 67.5 \times 10^3 electron/sec. \tag{33}$$

When adding the veto monitor cut, the Møller event rate will be reduced to:

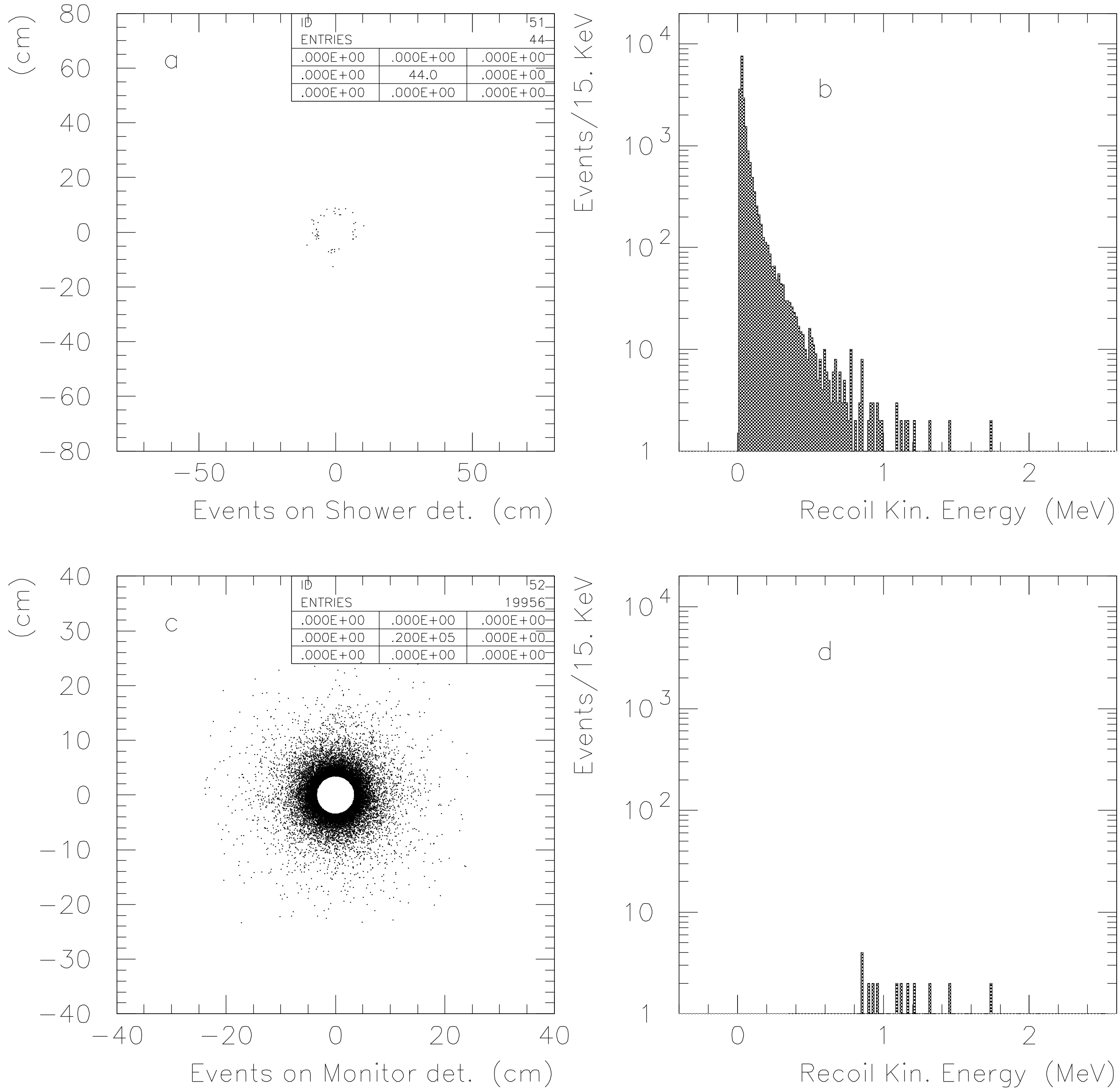

Figure 16: Monte Carlo simulation for $(e,^{12}C)$ elastic background

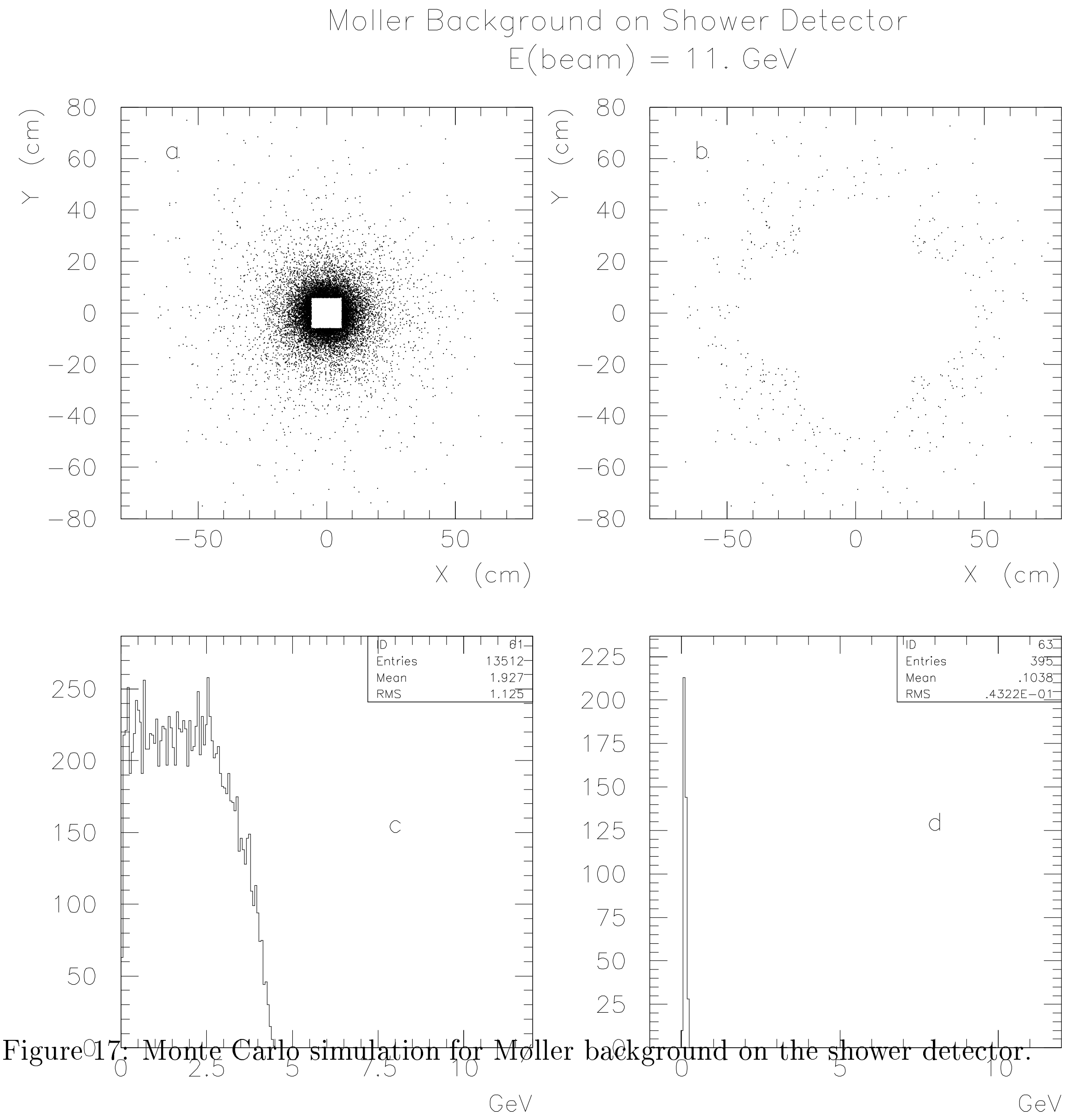

Figure 17: Monte Carlo simulation for Møller background on the shower detector.

$$
\begin{aligned}
N'_m &\sim 1. \times 10^5 \times \frac{400}{20 \times 10^3} && (34)\\
&\sim 2 \times 10^3 electron/sec && (35)
\end{aligned}
$$

The Møller event rate on veto monitor detector is $\sim 2 \times 10^5$ electron/sec.

In summary, implementing the background veto monitor detector will greatly help to reduce both elastic and Møller background in the recoil detector and the hybrid calorimeter.

3.4 Rates and Uncertainties

One can ensure a clean separation of the Primakoff mechanism from background photoproduction processes by exploiting the known Primakoff cross section's energy, Z^2, and angular dependence. As such, we propose measurements on different nuclei (^4He and ^{12}C discussed here), a range of energies, and over a range of angles as determined by the hybrid calorimeter (HYCAL).

Figure 3.3.4 shows a Monte Carlo simulation of the expected experimentally measured angular distribution of $\eta \to \gamma\gamma$ events on ^4He, where the resolution and geometrical acceptance of the hybrid calorimeter were taken into account. The target thickness was taken to be 2×10^{19} helium atoms/cm^2 and the calorimeter is $1.5m \times 1.5m$ and is 5 meters downstream of the target. Because the $\eta \to \gamma\gamma$ branching ratio is well known, the η is reconstructed by measuring 2γ in the calorimeter. The simulation corresponds to 30 days of beamtime at $5\mu Amps$, and yields 20,500 $\gamma\gamma$ events. A fit to these data results in a $\Gamma^{\eta}_{\gamma\gamma} = 0.4603$keV with a 1.8% statistical error. In comparison, the data were generated using the value from the Particle Data Book of 0.463 keV.

A Monte Carlo simulation of η production on ^{12}C was also performed (see figure 19) assuming a target thickness of 2×10^{19} carbon atoms/cm^2 where the carbon atoms are in the form of the heptane wire chamber gas. As with the previous simulation, the calculation corresponds to $5\mu Amps$ of beam current for 30 days. It is worth noting, however, that with the proposed setup involving recoil detection with low pressure multiwire proportional counters, where the chamber working gas heptane will be used as a target, the helium and carbon data would be obtained simultaneously. The simulation yields 72,500 $\eta \to \gamma\gamma$ events and gives a 0.7% statistical error on the width. The estimated experimental uncertainties for $\Gamma(\eta \to \gamma\gamma)$ is listed in the table 2.

For the η', we will directly use the missing mass reconstructed by recoil detection to identify the η', because of the poor knowledge of η' decay branching ratios. One γ registered in the calorimeter will be required in the trigger to cut off the background, such as ρ photoproduction. Figure 20 shows the simulated missing mass spectrum with all physical backgrounds except multi-pion production. The η' production rate will be similar to that of η. The estimated total error for the η' width is $\sim$ 3–4%.

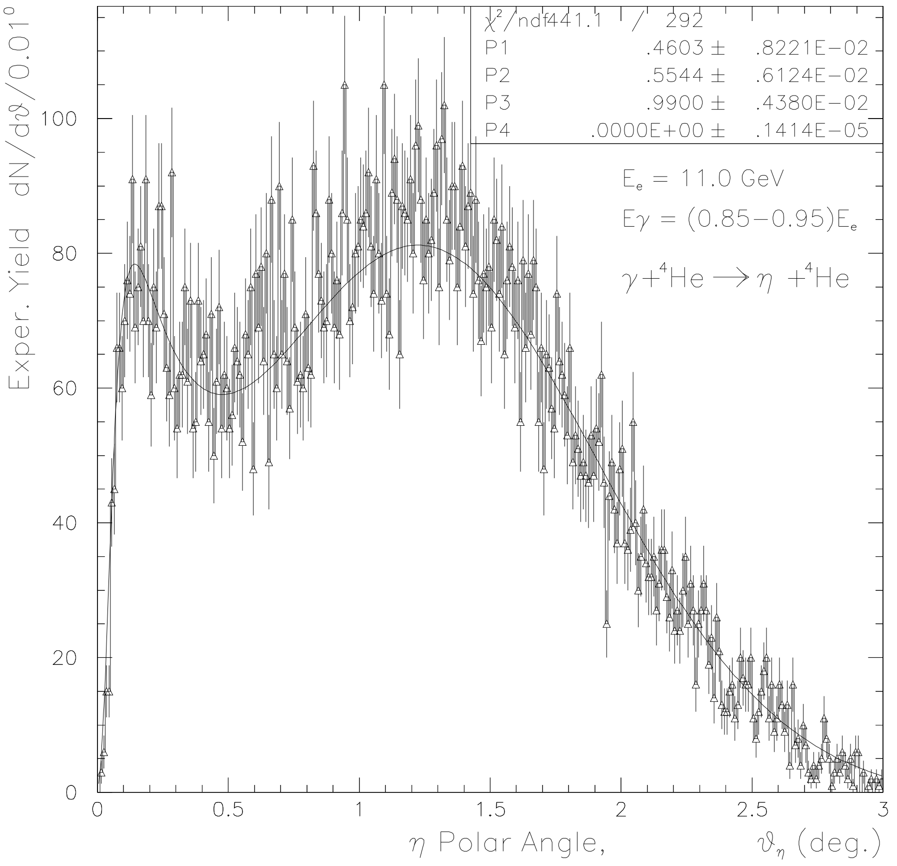

Figure 18: Monte Carlo simulation of experimentally measured angular distribution of $\eta\gamma\gamma$ events on ^4He.

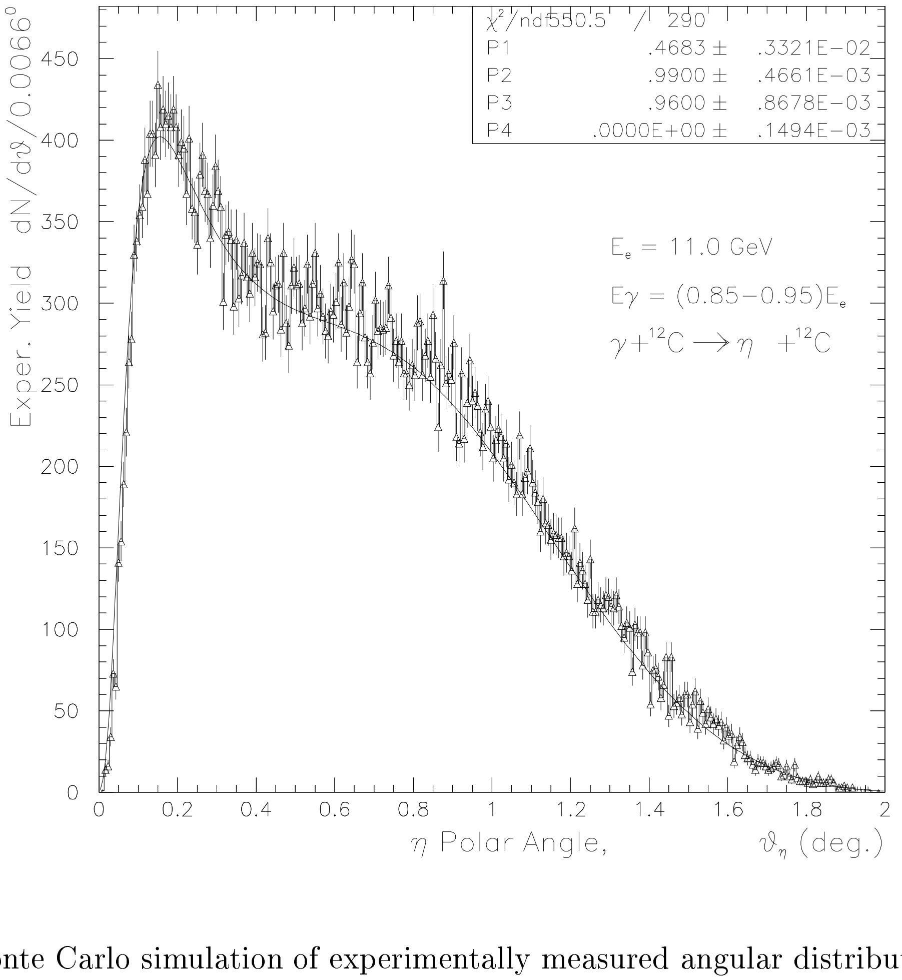

Figure 19: Monte Carlo simulation of experimentally measured angular distribution of $\eta\gamma\gamma$ events on ^{12}C.

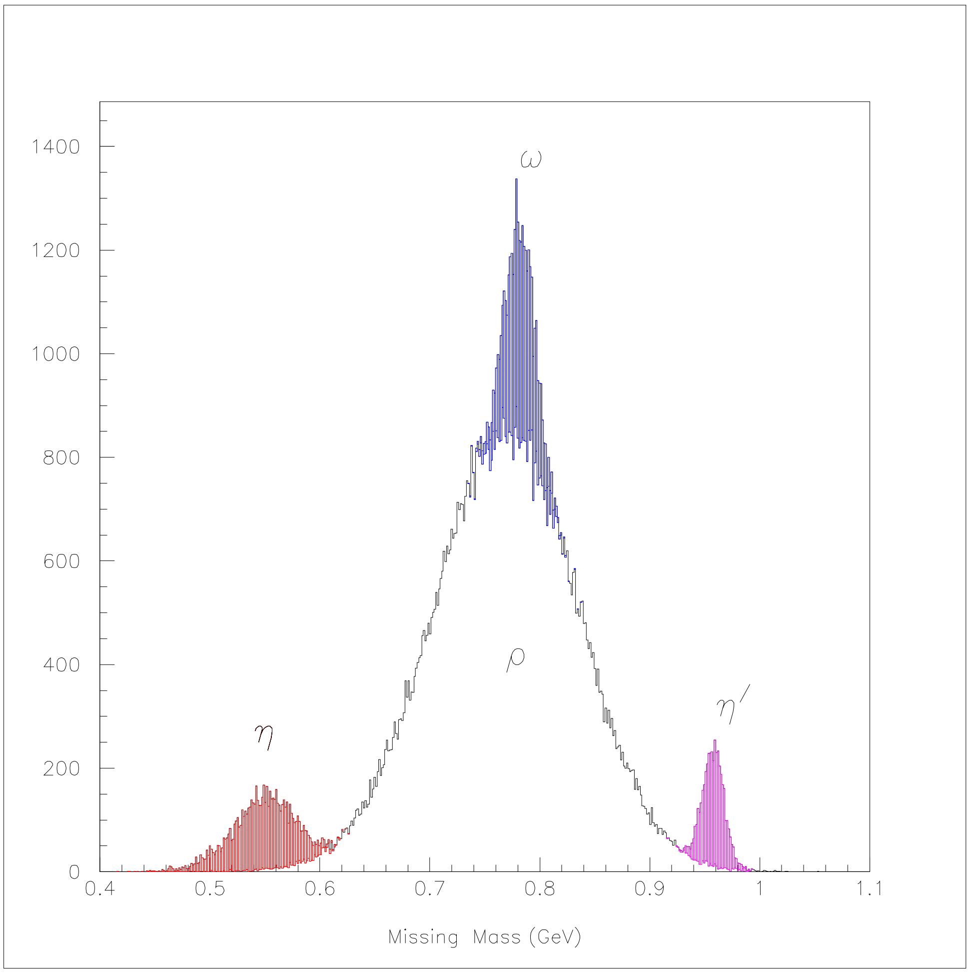

Figure 20: Monte Carlo simulation of the missing mass spectrum, with all backgrounds except multi-pion production.

Statistical	1.%
photon flux	1.%
target thickness	1.%
accptance, misalignment	0.4%
background subtract	0.3%
beam energy	0.2%
distorted form factor	0.3%
branching ratio	0.8% (PDB)
Total	2.0%

Table 2: Experimental uncertainties for $\Gamma(\eta \to \gamma\gamma)$ measurement.

3.5 Improvement on the η–η' Mixing Angle

As discussed earlier, the η–η' mixing angle is determined by:

$$\begin{aligned}\Gamma(\eta \to \gamma\gamma) &= \frac{\alpha_{\rm em}^2}{64\pi^3}\frac{M_\eta^3}{3f_\pi^2}\left[\frac{f_\pi}{\bar{f}_{\eta 8}}\cos\theta - \sqrt{8}\frac{f_\pi}{\bar{f}_{\eta 0}}\sin\theta\right]^2 , \\ \Gamma(\eta' \to \gamma\gamma) &= \frac{\alpha_{\rm em}^2}{64\pi^3}\frac{M_{\eta'}^3}{3f_\pi^2}\left[\frac{f_\pi}{\bar{f}_{\eta 8}}\sin\theta + \sqrt{8}\frac{f_\pi}{\bar{f}_{\eta 0}}\cos\theta\right]^2 .\end{aligned} \tag{36}$$

If one calculates the $\frac{f_\pi}{\bar{f}_{\eta 8}}$ using the leading log prediction of one-loop chiral perturbation theory[6]:

$$\frac{f_\pi}{\bar{f}_{\eta 8}} = 1 - \frac{m_k^2}{(4\pi f_\pi)^2}\ln\frac{m_k^2}{(4\pi f_\pi)^2} + \frac{m_\pi^2}{(4\pi f_\pi)^2} \tag{37}$$

where the experimental value of the pion decay constant is $f_\pi = 92.42 \pm 0.25$ MeV. Then $\frac{f_\pi}{\bar{f}_{\eta 0}}$ can be determined independent of the mixing angle from the π^0, η and η' two-gamma decay widths:

$$R \equiv \left[\frac{\Gamma(\eta \to \gamma\gamma)}{M_\eta^3} + \frac{\Gamma(\eta' \to \gamma\gamma)}{M_{\eta'}^3}\right]\frac{M_\pi^3}{\Gamma(\pi^0 \to \gamma\gamma)} = \frac{1}{3}\left(\frac{f_\pi^2}{\bar{f}_{\eta 8}^2} + 8\,\frac{f_\pi^2}{\bar{f}_{\eta 0}^2}\right) , \tag{38}$$

Therefore, the mixing angle can be calculated from equation 36.

If one uses the current average values of the π^0, η and η' two-gamma decay widths listed in the Particle Data Book: $\Gamma(\pi^0 \to \gamma\gamma) = 7.74 \pm 0.55$eV, $\Gamma(\eta \to \gamma\gamma) = 0.46 \pm 0.04$keV, and $\Gamma(\eta' \to \gamma\gamma) = 4.37 \pm 0.25$keV, the mixing angle and $\bar{f}_{\eta 0}$ will be:

$$\begin{aligned}\theta &= -20.75^o \pm 1.64^o \\ \bar{f}_{\eta 0} &= 1.08 \pm 0.05 f_\pi\end{aligned} \tag{39}$$

which indicates about an 8% error on the mixing angle and a 4.6% error on $\bar{f}_{\eta 0}$. On the other hand, if applying the 1.5% error on $\Gamma(\pi^0 \to \gamma\gamma)$ as proposed in the approved π^0 life time measurement experiment ($\Gamma(\pi^0 \to \gamma\gamma) = 7.74 \pm 0.11$eV), and 2% error on $\Gamma(\eta \to \gamma\gamma)$

as proposed in this experiment ($\Gamma(\eta \to \gamma\gamma) = 0.46 \pm 9.2 \times 10^{-3}$keV), while keeping the error on $\Gamma(\eta' \to \gamma\gamma)$ still the same as Particle Data Book average, with the central values of each width arbitrarily chosen to agree with the Particle Data Book average, one will get:

$$\begin{aligned} \theta &= -20.75^o \pm 0.61^o \\ \bar{f}_{\eta 0} &= 1.08 \pm 0.02 f_\pi \end{aligned} \tag{40}$$

It shows that the error on η–η' mixing angle reduces to $\sim 3\%$ and the error on $\bar{f}_{\eta_0}$ becomes $\sim 2\%$.

Furthermore, if using the error on the two-gamma decay widths of all three particles π^0,η and η' as suggested by this program: $\Gamma(\pi^0 \to \gamma\gamma) = 7.74 \pm 0.11$eV, $\Gamma(\eta \to \gamma\gamma) = 0.46 \pm 9.2 \times 10^{-3}$keV, and $\Gamma(\eta' \to \gamma\gamma) = 4.37 \pm 0.13$keV, the result would become:

$$\begin{aligned} \theta &= -20.75^o \pm 0.44^o \\ \bar{f}_{\eta 0} &= 1.08 \pm 0.01 f_\pi \end{aligned} \tag{41}$$

The η–η' mixing angle error would further reduce to $\sim$ 2% and the error on $\bar{f}_{\eta_0}$ would become 1.4%. As one can see, the proposed experimental program will significantly improve our understanding on both the η–η' mixing angle and the decay constant $\bar{f}_{\eta_0}$.

4 Measurements of the Transition Form Factors $F_{\gamma\gamma^* P}$

Studies of the $\gamma\gamma^* P$ vertex, where P represents the π^o, η, or η' pseudoscalar mesons and γ^* is a virtual photon of low or moderate Q^2, enable one to study the transition regime from soft nonperturbative physics to the hard processes of perturbative QCD. We propose to measure the photon momentum dependence of the form factors $F_{\gamma\gamma^* P}(Q^2)$ and thereby map out an extension to the axial anomaly to provide a clean test of QCD predictions for exclusive processes.

The structure of the meson's electromagnetic coupling is typically parameterized in the context of the vector meson dominance model in which a photon couples to hadronic matter via an intermediate vector meson. Such a model implies a form factor of the form:

$$F_\pi = \frac{1}{1 + q_\mu^2/m_V}, \tag{42}$$

where m_V is the mass of the vector meson. For the charged pion case, the Coulomb form factor has been measured[**?**] and the charge radius was determined to be about 0.6 fm. Due to charge conjugation symmetry, however, the elastic Coulomb form factor (γPP) vanishes. The $\gamma^*\gamma P$ transition vertex, on the other hand, is of great interest and has been studied theoretically from the point of view of models based on the VDM as well as those involving treatments of the quark substructure[**?**][**?**]. This transition is characterized by the form factor $F(q_1^2, q_2^2)$ which, if only one photon is significantly off shell, depends upon a form factor typically parameterized by the pole form (9), and approximated at low q_μ^2 by:

$$F_{\gamma^*\gamma\pi^o} \approx 1 - a\frac{q_\mu^2}{m_P^2}. \tag{43}$$

where a is a measure of the $\gamma^*\gamma P$ interaction radius.

The low, as well as high, Q^2 behavior of this form factor has been the source of considerable theortical efforts. As pointed out in Bijnens *et al.*, the next to leading order contributions are quite different when one of the photons is off shell. While the loop contributions tend to cancel when both photons are real, they have significant effect in the virtual case.

Recently, Maris and Tandy have used the ladder Bethe-Saltpeter solution for the dressed photon-quark vertex to study the low momentum behavior using model parameters fixed by the light meson masses and decay constants. They show that the often-used Ball-Chiu ansatz for the vertex is deficient. The results of their calculation are shown below, where the dot-dash line uses the bare vertex, the dashed is the Ball-Chiu ansatz, and the solid line is their calculation.

Frank, *et al.*, have calculated $F_{\gamma^*\gamma\pi^o}$ from a generalized impulse approximation within a QCD-based model field theory which gives a good description of the charged pion form factor. Their approach uses dressed vertices and propagators consistent with dynamical chiral symmetry breaking, gauge invariance, quark confinement, and perturbative QCD. Their results are shown below where they find a $\pi\gamma\gamma$ interaction radius of $0.47 fm$.

Ivanov and Lyubovitskij calculate the form factor within a Lagrangian quark model with a separable interaction known to provide a good description of the pion observables at low energies. With their gaussian pion-quark vertex, they obtain an $r_{\pi^o} = 0.65 fm$. Their results are indicated by the dashed line in the following figure.

Despite the theoretical interest in pseudscalar meson form factors, the experimental situation remains incomplete. Here, we indicate the experiments which have been performed, and the contributions which could be made with 11 GeV electron beams using the virtual Primakoff effect.

4.1 Previous Measurements in the Space-like Region

A number of experiments have been performed to measure these transition form factors. While great progress has been made in the high Q^2 region, data at low and intermediate regime are currently quite poor. The CELLO collaboration at PETRA has measured $F_{\gamma^*\gamma P}$ in the space-like region at large momentum transfers using the reaction $e^+e^- \to e^+e^- P$[**?**]. In this experiment two photons are radiated virtually by the colliding e^+e^- beams. One of the virtual photons is close to real and the other has a larger q_μ^2 and is tagged by the detection of an e^+ or e^-.

Measurements were taken at momentum transfers ranging from 0.62 to 2.17 $(GeV/c)^2$, and the value of a was deduced by extrapolation under the assumption of vector meson dominance. For the pion, the authors quote a value of $a = 0.0325 \pm 0.0026$ (statistical)

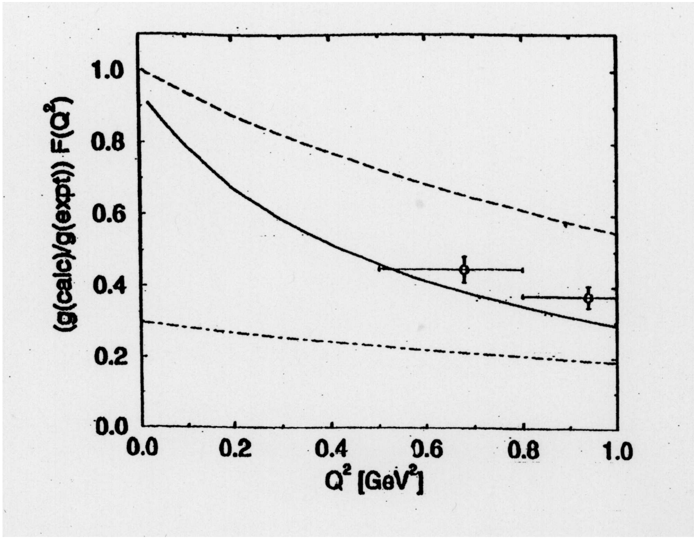

Figure 21: The $\gamma^*\gamma\pi^o$ transition form factor using a bare vertex (dot-dash), and the BC Ansatz (dashed) and the numerical solution of Maris and Tandy

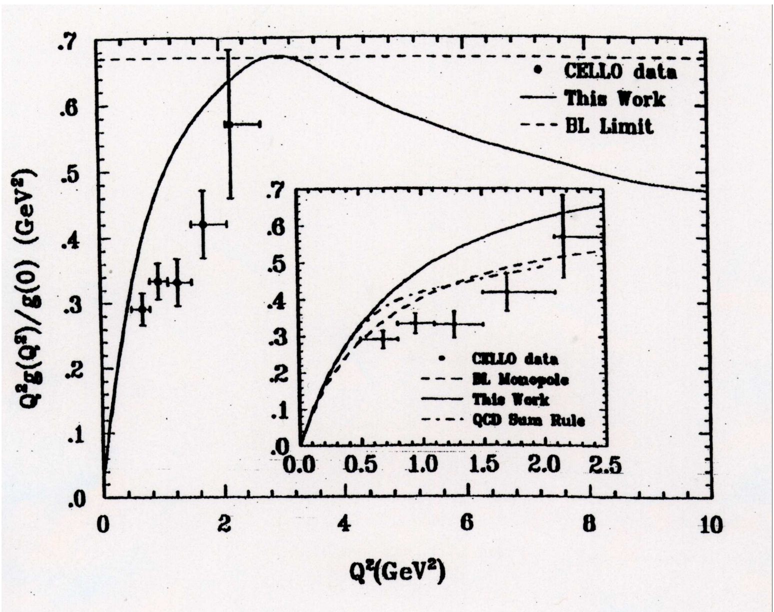

Figure 22: The $\gamma\gamma^*\pi^o$ form factor multiplied by Q^2. The data are from the CELLO Collaboration, and the solid line is the calculation of Frank. The dashed line is the pQCD factorization limit.

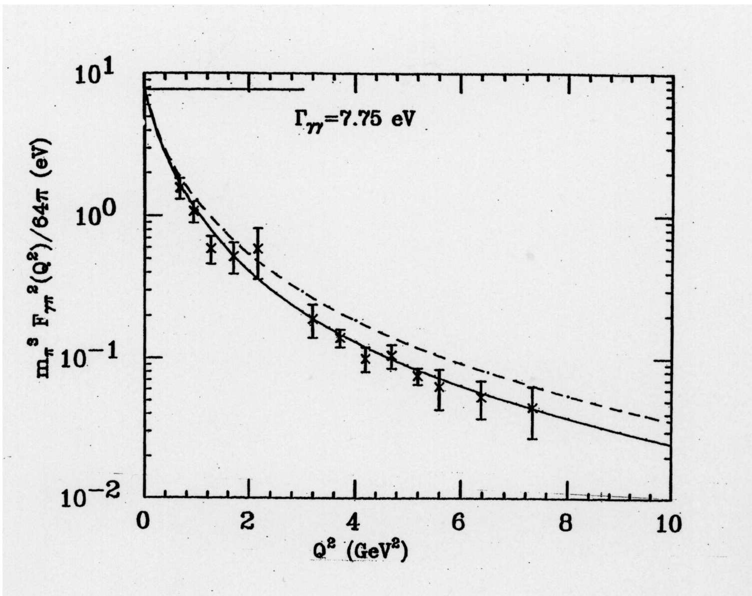

Figure 23: The $\gamma\gamma^*\pi^o$ form factor as calculated by Ivanov and Lyubovitskij. The data are from the CELLO and CLEO Collaborations.

with systematic errors estimated to be of the same order as the statistical error. The results of these measurements are shown in figure 24 with the corresponding fit to $F_{\gamma^*\gamma P}$. From the plot, it is clear that any extraction of the slope parameter at $Q^2 = 0$ is highly model dependent. Data covering the higher q_μ^2 region from 2 to 20 GeV^2 have also been reported by the CLEO collaboration[?]. High Q^2 measurements on the η and η' have been performed as well.

A conditionally approved experiment in Hall A (E97-009) will measure this form factor in the very low q_μ^2 regime ranging from 0.005 to about 0.035 $(GeV/c)^2$ to extract a. This leaves the intermediate momentum transfer region for the pion largely unexplored experimentally. While the L3 Collaboration has some results (with very poor Q^2 resolution) in the low Q^2 region for the η', low and intermediate Q^2 data on the η are totally lacking. The advent of 11 GeV electrons at TJNAF, however, will make such studies possible.

4.2 Previous Experiments in the Time-like Region

A number of experiments aimed at measuring a have been performed in the time-like momentum transfer region utilizing the π^o and η Dalitz decay $\pi^o/\eta \to e^+e^-\gamma$ reaction[3-12] The amplitude for this process involves the $F_{\gamma^*\gamma\P}$ form factor which, in the usual linear expansion

$$F(x) \approx 1 + a\frac{m_{e^+e^-}^2}{m_P^2}. \tag{44}$$

a	reference
$+0.025 \pm 0.014 \pm 0.026$	Meijer Drees, 1992 [?]
$+0.026 \pm 0.024 \pm 0.048$	Farzanpay, 1992 [?]
$-0.11 \pm 0.03 \pm 0.08$	Fonvielle, 1989 [?]
$-0.01 + 0.08 - 0.06$	Gumplinger, 1987 [?]
$0.12 + 0.05 - 0.04$	Tupper, 1983 [?] (reanalysis of [?])
$+0.10 \pm 0.03$	Fischer, 1978 [?]
$+0.02 \pm 0.1$	Burger, 1972 [?]
$+0.01 \pm 0.11$	Devons, 1969 [?]
-0.24 ± 0.16	Samios, 1961 [?]
-0.15 ± 0.10	Kobrak, 1961 [?]

A summary of these measurements on the pion is shown in the table above, where it can be seen that the published values for the slope range from -0.24 to $+0.12$. Such experiments suffer from small kinematically accessible ranges and significant backgrounds, and they require large final-state radiative corrections. As such, these experiments have not been able to determine even the sign of the form factor slope.

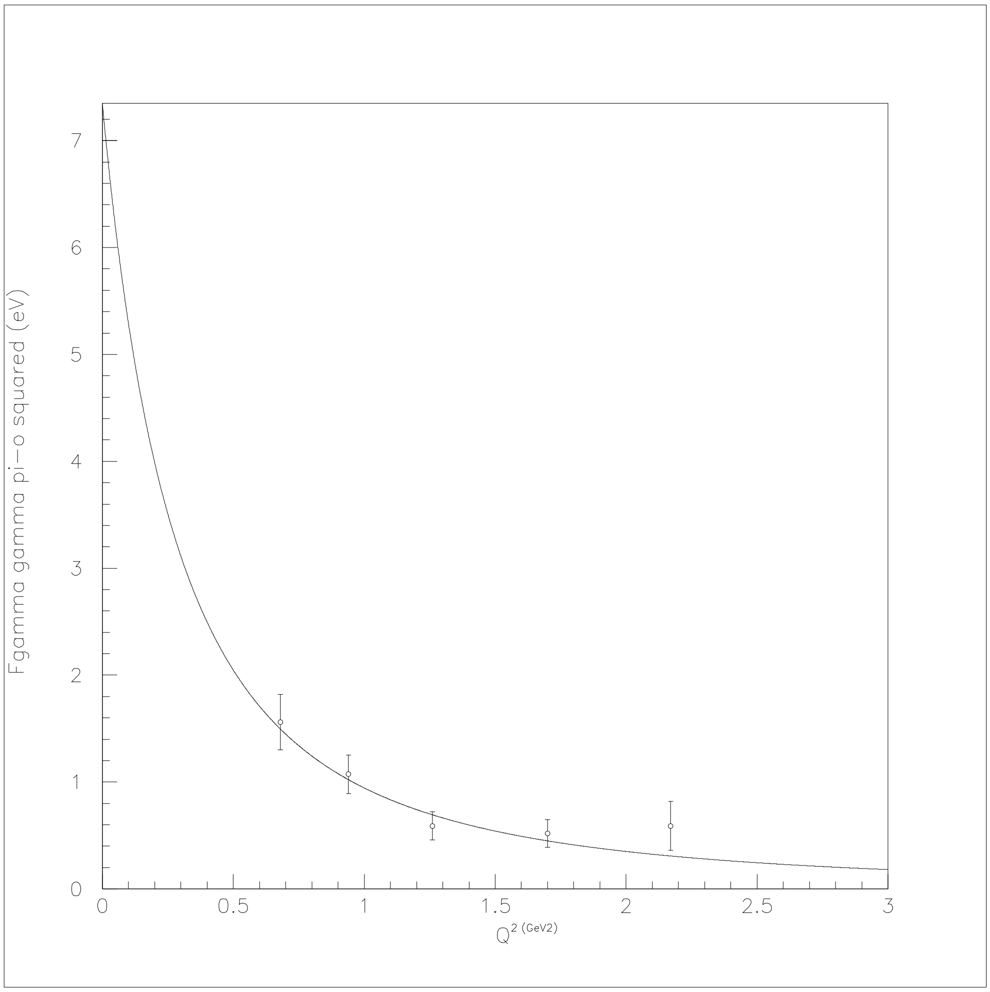

Figure 24: $F_{\gamma\gamma^*\pi^o}$ as measured by the CELLO Collaboration, with the low Q^2 extrapolation based on vector meson dominance.

4.3 The Proposed Experiment

In 1989, Hadjimichael and Fallieros[?] suggested that the virtual Primakoff effect could access additional fundamental information about the pion as the cross section is proportional to $|F_{\gamma^*\gamma\pi^o}(q_\mu^2)|^2$. The full expression for the virtual Primakoff scattering cross section is[?][?]:

$$\begin{aligned} \frac{d^3\sigma}{d\epsilon_2 d\Omega_2 d\Omega_\pi} &= \frac{Z^2\eta^2}{\pi}\sigma_M \frac{Q^4}{K^4}\frac{\beta_\pi^{-1}}{\omega_\pi}|F_N(K^2)|^2|F_{\gamma^*\gamma\pi^o}(q_\mu^2)|^2 sin^2(\frac{\theta_e}{2})sin^2(\theta_\pi) \\ &\times[4\epsilon_1\epsilon_2 sin^2\phi_\pi + |\vec{q}|^2/cos^2(\frac{\theta_e}{2})] \end{aligned} \tag{45}$$

where σ_M is the Mott cross section, $\eta^2 = (4/\pi m^3)/\tau$, τ is the π^o lifetime, K is the (nearly real) photon four momentum from the Coulomb field, the pion four momentum is $Q = (\vec{q}, \omega_\pi)$, $\beta_\pi = \vec{q}/\omega_\pi$, and $F_N(K^2)$ is the nuclear form factor. This expression for the cross section in similar to that for the real Primakoff effect, with the notable exception of the form factor $|F_{\gamma^*\gamma\pi^o}(q_\mu^2)|^2$ which is of interest here.

Hadjimichael and Fallieros examined the sensitivity of the cross section to a for energy transfers up to 1.6 GeV. They saw only moderate sensitivity and noted that the cross section is optimized for $\theta_e \to 0$ and $\theta_\pi \to 0$ whereas pion energies above 2 GeV are favored for probing the $\gamma^*\gamma\pi^o$ vertex. We have extended these calculations to kinematical regimes available with the proposed 11 GeV electron beam at TJNAF and note that good sensitivity to the $\gamma^*\gamma P$ form factor is present.

Figure 25 shows the cross sections for the virtual Primakoff pion photoproduction process on helium-4 as a function of $E_{e'}$, an electron scattering angle of 2 degrees and a pion angle of 0.1 degrees with respect to $\vec{q}$. The incident energy is 11 GeV. The two curves are for the VDM prediction ($a = 0.03$) and that using the slope parameter determined by the $\pi^o \to e^+e^-\gamma$ experiment ($a = 0.1$) of reference [?]. From the plot one can see that the cross sections are large, and are quite sensitive to the pion transition form factor. If we define a figure of merit to be the difference in the predicted cross section for the two form factors times the square root of the average cross section, figure **??**, we see that the optimal kinematics are at θ_e=2 degrees and $\omega \approx 6$ GeV.

4.3.1 Experimental Setup for Transition Form Factor Measurements

We have investigated the Q^2 acceptance available for an experimental setup in which both the scattered electron and the two photons from the meson decay are detected in the previously described hybrid calorimeter (see figure 27). The calorimeter is $1.5m \times 1.5m$, is $7m$ downstream of the target, and has a $12cm \times 12cm$ central hole to allow the beam to pass through. For such a setup, the phase space for Q^2 acceptance is shown in figure 28 where a 1 GeV energy cut has been imposed on the scattered electron and the incident beam energy is 11 GeV. If one restricts the electron scattering angle and energy transfer to regions in which the figure of merit is largest (θ_e between 0.5 and 6 degrees, ν between 2 and 10 GeV), one obtains the Q^2 phase space shown in figures 29 and 30, where figure 30 shows the very low Q^2 acceptance. It can be seen that this setup complements the CELLO measurements in covering the extremely low Q^2 region which is unavailable to the collider experiments.

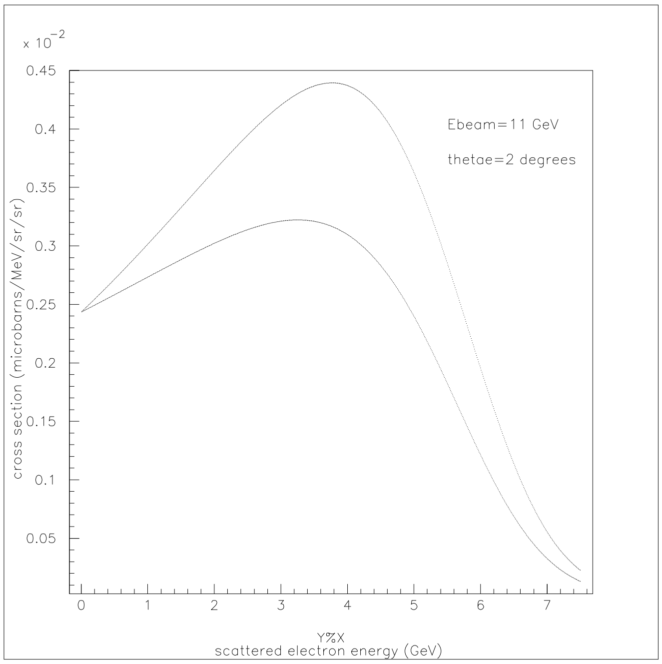

Figure 25: Cross section *verses* scattered electron energy for π^o production on helium-4. The incident electron energy is 11 GeV.

Figures 31 and 32 show the resolutions in Q^2 at $Q^2 = 0.01 GeV^2$ and $Q^2 = 0.5 GeV^2$, respectively, resulting from finite position and energy resolutions in the detection of the scattered electrons in the hybrid calorimeter. It can be seen that the Q^2 resolution is more than adequate to extract the Q^2 dependence of $F_{\gamma\gamma^* P}$.

4.3.2 Rates for $F_{\gamma\gamma^*\pi^o}$ and $F_{\gamma\gamma^*\eta^o}$

Figure 33 shows the cross section as a function of θ_π for Primakoff, coherent nuclear, and interference photoproduction processes. It can be seen that clean separation is possible. The analogous curves for the η figure of merit and cross section are shown in figures 34 and 35.

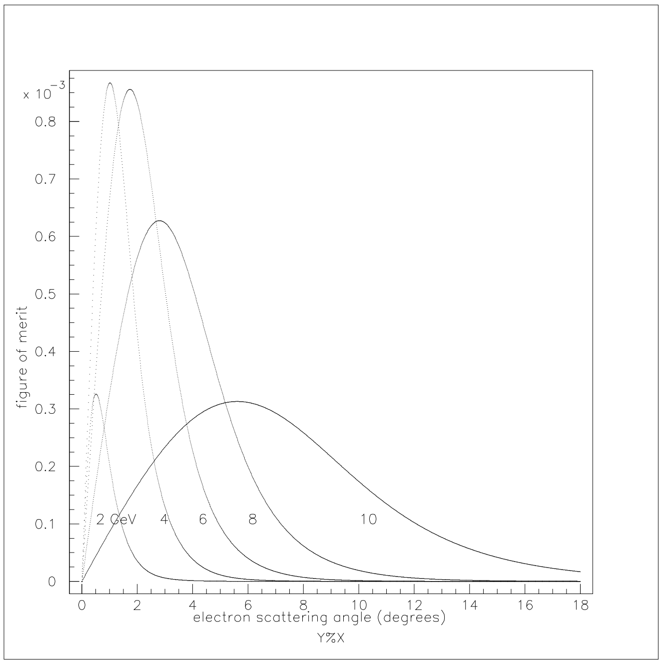

Figure 26: Figure of merit (see text) *verses* electron scattering angle for π^o production on helium-4. The incident electron energy is 11 GeV, and the various energy transfers are indicated.

With this experimental setup, we expect a yield of 3900 π^o's and 600 η's per day. This assumes a 10^{-5} radiation length ^4He target, and a $5\mu Amp$ 11 GeV electron beam. The two photon acceptance of the hybrid calorimeter was taken to be 50%, and the branching ration for two photon decay of the η was taken to be 39%.

5 Summary

We have described a comprehensive program to measure the electromagnetic properties of pseudoscalar mesons which would be possible with advent of 11 GeV CW electron beams at Jefferson Lab. Precise measurements of the two photon widths and transition form factors would provide stringent tests of both QCD and QCD based models. We believe the proposed instrumentation to be constructed for this program will be of general use to both this program, and future experiments.

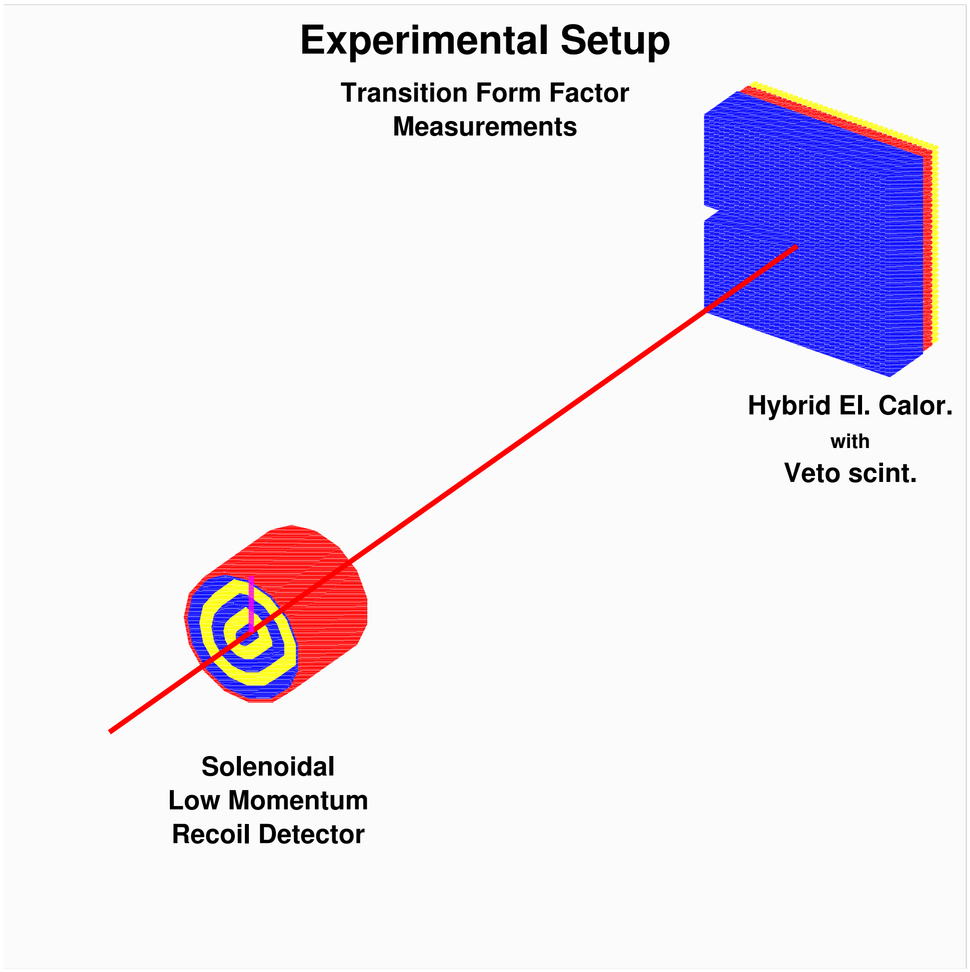
Experimental Setup
Transition Form Factor
Measurements
Hybrid El. Calor.
with
Veto scint.
Solenoidal
Low Momentum
Recoil Detector

Figure 27:

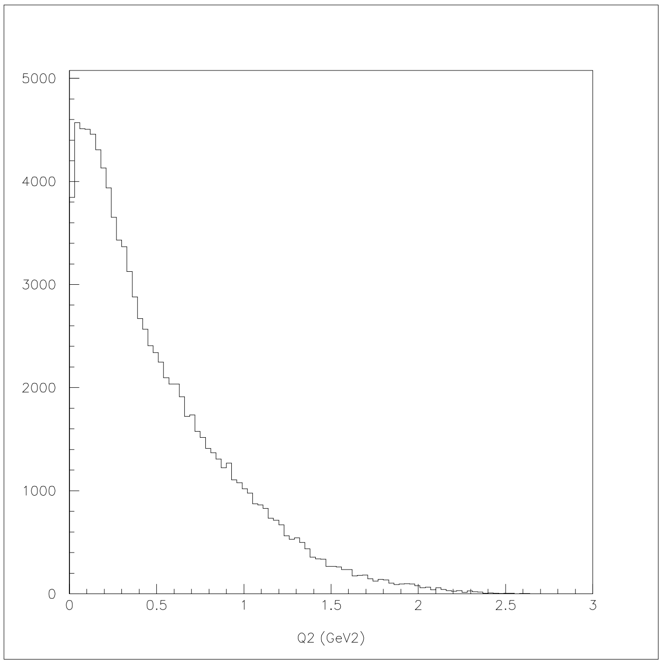

Figure 28: Phase space for Q^2 acceptance of a $1.5m \times 1.5m$ detector with a $12cm \times 12cm$ central hole. Detector is 7 m from target. A 1 GeV energy cut is imposed.

References

[1] J.S. Bell et al., Il Nuovo Cimento, vol. 51, no. 1., (1969), 4

[2] S. Adler, Phys. Rev., vol. 177, no. 5, (1969), 2426.

[3] F. Anulli *et al.*, p. 607 in Vol. II of *The second DAΦNE physics handbook*, edited by L. Maiani *et al.*, published 1995 by INFN - LNF - Divisione Ricerca, ISBN 88-86409-02-8

[4] International workshop on the structure of the η' meson, March 8–9, 1996, edited by M. Burkardt, J. Goity, V. Papavassiliou and S. Pate, World scientific.

[5] V.V. Anisovich et al, Phys.Lett.B404(1997)166.

[6] B. Holstein et al, Phys. ReV. D57(1998)4397.

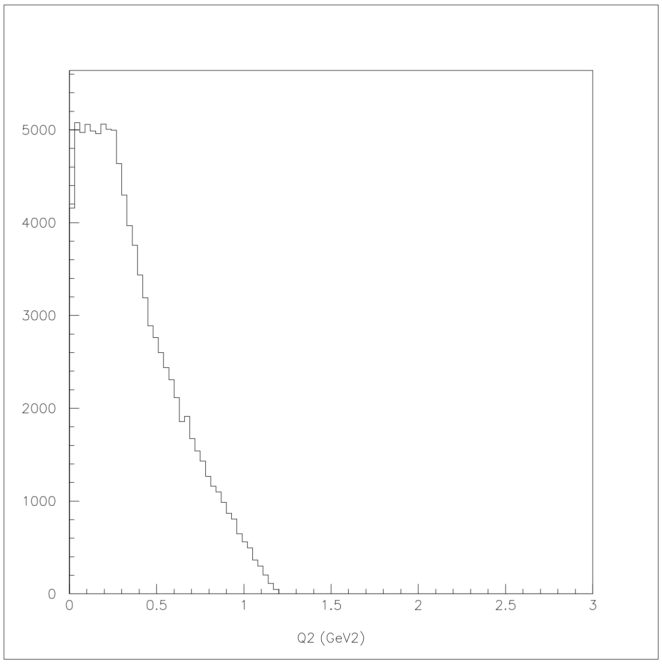

Figure 29: Phase space for Q^2 acceptance of a $1.5m \times 1.5m$ detector with a $12cm \times 12cm$ central hole. Detector is 7 m from target. Scattering angle is between 0.5 and 6 degrees. Energy transfer is between 2 and 10 GeV.

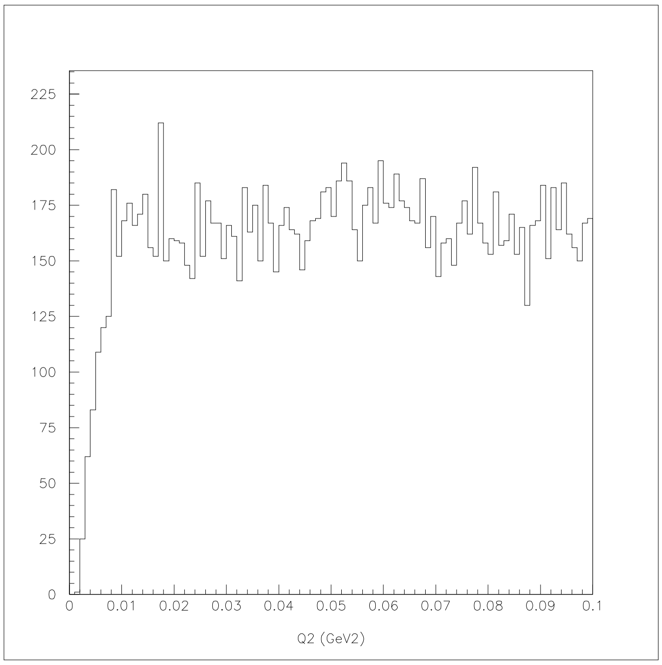

Figure 30: Phase space for Q^2 acceptance of a $1.5m \times 1.5m$ detector with a $12cm \times 12cm$ central hole. Detector is 7 m from target.Scattering angle is between 0.5 and 6 degrees. Energy transfer is between 2 and 10 GeV.

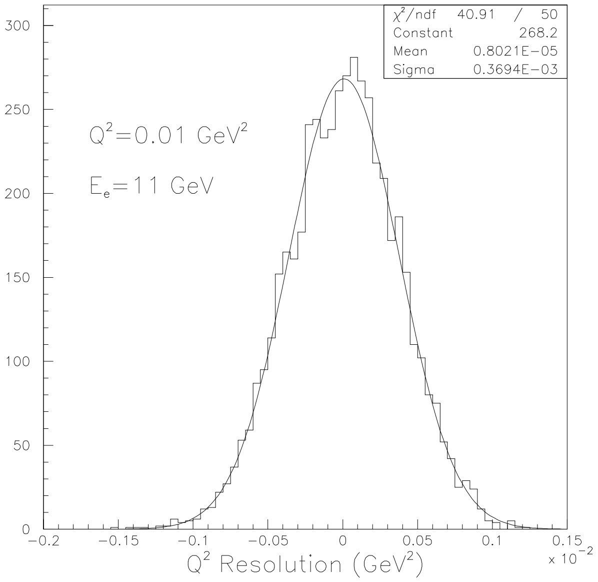

Figure 31: The diference in actual *verses* reconstructed Q^2 resolution for $Q^2 = 0.01 GeV^2$.

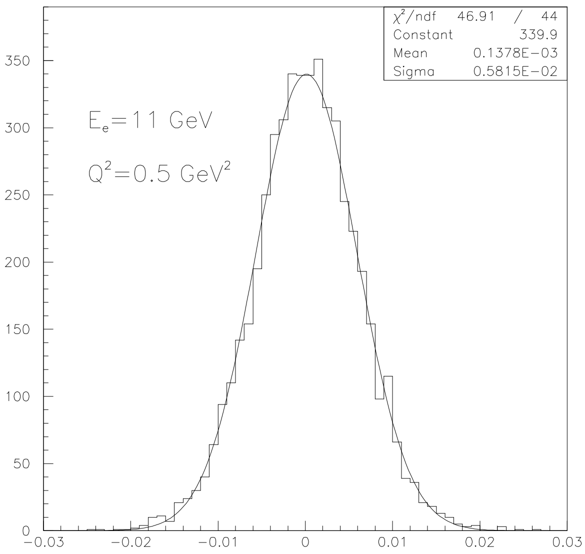

Figure 32: The diference in actual *verses* reconstructed Q^2 resolution for $Q^2 = 0.5 GeV^2$.

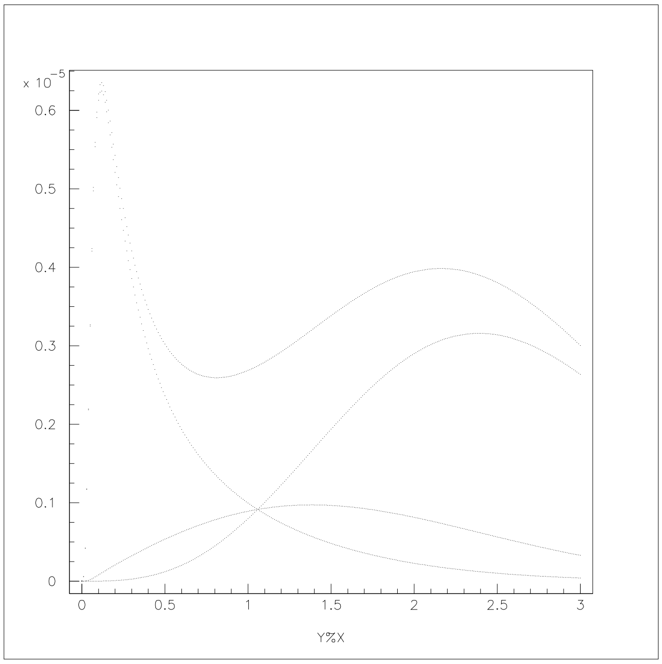

Figure 33: Cross section *versus* θ_π weighted by $sin(\theta_\pi)$ showing Primakoff, nuclear coherent, and their interference.

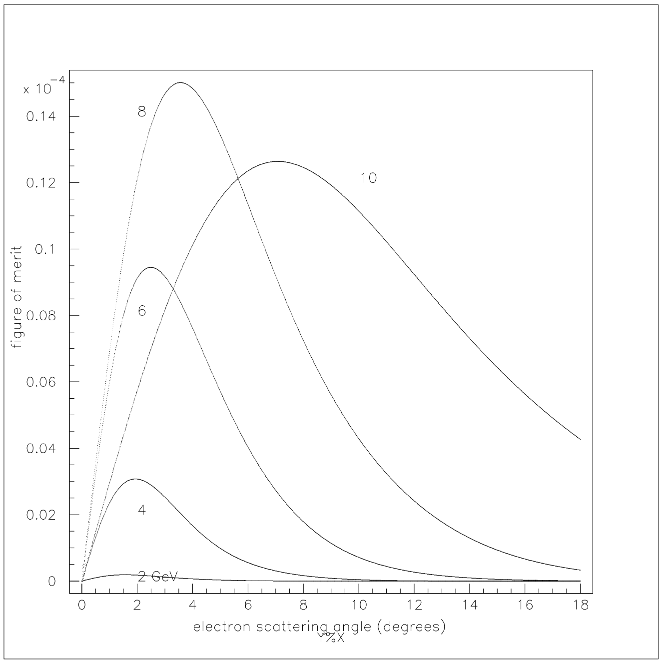

Figure 34: Figure of merit (see text) *verses* electron scattering angle for η production on helium-4. The incident electron energy is 11 GeV, and the various energy transfers are indicated.

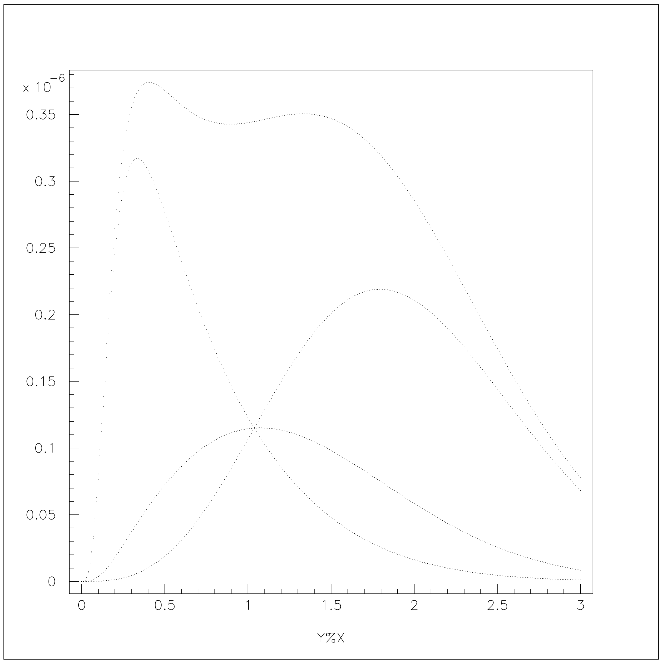

Figure 35: Cross section *versus* θ_η weighted by $sin(\theta_\pi)$ showing Primakoff, nuclear coherent, and their interference.